

Effect of filter type on the statistics of energy transfer between resolved and subfilter scales from a-priori analysis of direct numerical simulations of isotropic turbulence

M. Buzzicotti¹, M. Linkmann¹, H. Aluie², L. Biferale¹, J. Brasseur³ and C. Meneveau⁴

¹Dept. of Physics and INFN, University of Rome Tor Vergata, Rome, Italy

²Dept. of Mechanical Engineering, University of Rochester, USA

³Aerospace Engineering Sciences, University of Colorado, Boulder, USA

⁴Dept. of Mechanical Engineering, The Johns Hopkins University, Baltimore, USA

ARTICLE HISTORY

Compiled Friday 23rd February, 2018

ABSTRACT

The effects of different filtering strategies on the statistical properties of the resolved-to-subfilter scale (SFS) energy transfer are analysed in forced homogeneous and isotropic turbulence. We carry out *a priori* analyses of the statistical characteristics of SFS energy transfer by filtering data obtained from direct numerical simulations with up to 2048^3 grid points as a function of the filter cut-off scale. In order to quantify the dependence of extreme events and anomalous scaling on the filter, we compare a sharp Fourier Galerkin projector, a Gaussian filter and a novel class of Galerkin projectors with non-sharp spectral filter profiles. Of interest is the importance of Galilean invariance and we confirm that local SFS energy transfer displays intermittency scaling in both skewness and flatness as a function of the cut-off scale. Furthermore, we quantify the robustness of scaling as a function of the filtering type.

KEYWORDS

isotropic turbulence, large eddy simulation

1. Introduction

Understanding and predicting multiscale turbulent statistics are key challenges for many modern applied and fundamental problems in fluid turbulence dynamics. Of major interest is the existence of intermittency [1–3], i.e. the development of anomalously intense fluctuations that depart more and more from Gaussianity by going to smaller and smaller scales [1]. Similarly, the statistics of velocity gradients become increasingly intermittent by augmenting the turbulent intensity, generally expressed by the Reynolds number, a measure of the relative importance of non-linear and linear terms in the three dimensional Navier-Stokes equations. Anomalous multiscale fluctuations are generic in three-dimensional (3D) turbulence, being observed at small scales in homogeneous and inhomogeneous flows such as wall-bounded flows [4–9] and also in Lagrangian statistics [10–15]. The Reynolds numbers attainable in direct numerical simulations (DNS) are still far below those occurring in nature and in most engineering

applications. Hence, modelling is often unavoidable, and one of the commonly used approaches is based on large eddy simulation (LES) [2,3,16–18].

The basic idea of LES is to advance the turbulence dynamics on a coarse-grained grid with resolution sufficient to capture a large percent of the turbulent kinetic energy (and variances in other key fluctuating variables). Thus, models are required to capture dominant effects of the subfilter-scale (SFS) motions on resolved large-scale dynamics. In this paper, we focus primarily on the impact of the details of the filter type on the statistics of the resolved-scale, both at the energy-containing range and close to the filter scale. We do this using only physical-space data from fully resolved DNS by analysing physical space SFS statistics without introducing any modelling (*a-priori* analysis [19]).

LES aims to predict integral-scale variables, where kinetic energy is concentrated, to acceptable degrees of accuracy. In practice, the accuracy of the SFS model is generally assessed in terms of its ability to achieve good agreement with empirical measurements of one-point or two-point statistics such as mean profiles, energy spectra and the Reynolds stress tensor. On the other hand, it is well known that LES has special difficulties near solid boundaries, where key integral length scales are proportional to the distance from the wall and integral-scale motions tend to become under-resolved, and where small-scale energy and vorticity injections/ejections directly impact the mean flow [2,9,20–24]. The most common LES models replace the SFS stress tensor with an eddy viscosity form that replaces the true inertial resolved-SFS dynamics with a form that is diffusive in momentum and dissipative in energy. Hence, the inertial (time reversible) contribution to the resolved-to-SFS dynamics is everywhere approximated as a dissipative loss [16]. It is increasingly common for LES to be applied at relatively high resolution with the filter scale well within the inertial subrange [25,26]. In such cases, there is a need to go beyond first- and second-order statistics to validate/benchmark the LES accuracy in relationship to the presence of strong non-Gaussian fluctuations and of resolved-to-SFS interactions at the smallest resolved scales [27], which might even lead to backscatter events [28–33]. Moreover, the need to apply LES to study Lagrangian evolution of small particles or to the advection/reaction of Eulerian fields (combustion, multicomponent flows, etc.), calls for refined control of the impact of the modelled SFS stress tensor on the multiscale statistical properties of the predicted resolved velocity field. Furthermore, in many important turbulent flows, a global backward cascade with a mean negative energy transfer in the domain exists. This is the case with fast rotating flows [34–36] and shallow fluid layers [37–41]. In certain circumstances of conducting flows [42,43], the backward-*cascading* quantity is the magnetic helicity, which results in some energy also being *transferred* from small scales to large scales if the magnetic helicity is nonzero.

The first goal of this paper is to present a systematic investigation of the key statistical properties of SFS energy transfer that the modelled SFS stress tensor should reproduce in order to capture intense non-Gaussian SFS fluctuations, including those responsible for back-scatter. We do that by performing an *a priori* study of the multiscale properties of SFS energy transfer from high-resolution DNS on up to 2048 collocation points per spatial direction. In particular, we aim to define a set of benchmarks for future high-resolution LES of high Reynolds number turbulence where an inertial subrange of turbulence scales exists and is well resolved, so that strong intermittency close to the SFS cut-off creates large departures from Gaussian statistics.

In LES where intermittency at the smallest resolved scales is of interest, benchmarking the LES model will require evaluation of multi-point statistics of order higher than second (i.e., beyond (co)variances, spectral properties, correlation functions, etc.). In

previous work [44], intermittency and non-Gaussian properties of the SFS energy transfer were analysed at moderate resolution and by using extended self similarity (ESS) [45,46], showing that SFS energy transfer statistics are affected by non-trivial anomalous deviations from the classical scaling as a function of the cut-off scale. Here, we follow the same approach but we focus on the impact of the filter and extend the analysis to much higher Reynolds numbers and by changing the filter properties (see as follows).

Another motivation for the current analysis is based on more fundamental aspects. It is usually thought that the inertial spectral properties in fully developed homogeneous turbulence are asymptotically independent of the way energy is absorbed at high wavenumbers, i.e. if the Reynolds number is large enough, the inertial-range statistics of second-order velocity correlation functions are independent of the mechanism by which energy is transferred and absorbed at the small scales since the interactions distributing the kinetic energy are mostly local in scale [47–49].

This is the main motivation behind the introduction of hyperviscosity in many numerical studies [50]. However, in LES, the statistics at the smallest resolved scales can certainly depend on the details of the SFS model. Since higher-order moments have a non-local support in Fourier space, one would expect that they might become progressively more sensitive to the details of the model for the SFS stress tensor. A natural question then arises: is it possible to devise a LES scheme which *minimises* the cut-off effects on the resolved inertial range, achieving a scaling as extended as possible for high-order correlation functions too? Improved closures that also predict intermittency would be helpful also to LES practitioners with a need to push the SFS cut-off to scales small enough where intermittency effects are important.

Being interested in intense-but-rare statistical properties, we need first to define a set of SFS observables which are statistically robust and not strongly affected by filter-induced effects and/or fluctuations induced by coupling among the resolved scales. To this end, we apply a filter formalism that isolates the terms that genuinely couple resolved and unresolved scales from those that are affected by other contributions due to self-coupling of the resolved fields. Moreover, we discuss in detail the importance of focusing on Galilean invariant quantities, in order to avoid strong contamination from unphysical fluctuations affecting the very intense events (and not the mean single-point properties) [48,49,51].

In what follows, we carry out an *a priori* analysis of the different components of the SFS energy transfer by filtering DNS data with different filter thresholds. Since LES results depend not only on the details of the SFS-model but also on the choice of the filter, and since the filter-induced fluctuations will vary, we are particularly interested in sensitivity to different filtering types and procedures. Beside the standard sharp Fourier Galerkin projector and a convolution with a Gaussian kernel, we also devise a novel class of Galerkin filters with a non-sharp probabilistic profile in Fourier space. The set of new projectors offer multiscale filtering in Fourier space while maintaining formal and practical advantages specific to projector filters.

The analysis is structured as follows. We begin in section 2 with a brief description of the DNS database and the numerical methods applied to generate and analyse the data. In sec. 3, we motivate and introduce the filtering formulation and investigate the properties of different filter-dependent components of SFS energy transfer under Galilean transformations. We show that an apparent breaking of Galilean invariance of the SFS-energy transfer term can be remedied by introducing a more refined distinction between the contributions to the SFS energy transfer which require modelling and those which do not. The first results from the *a-priori* analysis are presented in sec. 4,

where we measure the fluctuations of different components of the SFS energy transfer. We provide measurements of intermittent scaling of the SFS energy transfer at high Reynolds numbers without using ESS. Section 5 is dedicated to an analysis of different filtering procedures on the statistics of SFS energy transfer and we introduce a novel class of Galerkin filters with a non-sharp profile in Fourier space. We summarise our results in sec. 6.

2. Description of the data-sets

Data id	N	Re $_{\ell}$	ε	U	ℓ	ν	α	T_0/T_{eddy}
V1	1024	2570	1.9	1.8	1.2	0.0008	1	25
V2	2048	7000	1.4	1.5	1.2	0.0003	1	9
H1	1024	8000	1.9	1.9	1.3	2×10^{-8}	2	7
H2	2048	26000	1.5	1.6	1.1	5.7×10^{-20}	4	6

Table 1. The identifiers V and H distinguish between hyper and normal viscosity, where α is the order of the Laplacian. N denotes the number of grid points in each Cartesian coordinate, U the rms velocity, $\ell = (\pi/2U^2) \int dk E(k)/k$ the integral scale, ν the kinematic viscosity, ε the dissipation rate and T_0/T_{eddy} the steady-state run time in units of large-eddy turnover time $T_{\text{eddy}} = \ell/U$. The values given for ε , U , ℓ are time averages. The integral-scale Reynolds number is $\text{Re}_{\ell} = U\ell/\nu$ for data-set V while for the hyperviscous simulations it is defined as $\text{Re}_{\ell} = C(\ell/l_d)^{4/3}$, where C is a constant estimated by comparing the two definitions for data-set V and l_d is the scale corresponding to the maximum of $k^2E(k)$, see Figure 1 (b).

In order to generate the data-sets for the *a priori* analysis, we numerically solved the 3D Navier-Stokes equations using both normal and hyperviscosity

$$\partial_t \mathbf{v} = -\nabla \cdot (\mathbf{v} \otimes \mathbf{v}) - \nabla p + \nu(-1)^{\alpha+1} \Delta^{\alpha} \mathbf{v} + \mathbf{f} , \quad (1)$$

$$\nabla \cdot \mathbf{v} = 0 , \quad (2)$$

where \mathbf{v} denotes the velocity field, p is the pressure divided by the constant density, ν the kinematic viscosity, \mathbf{f} an external force and α the power of the Laplacian. As indicated in Table 1, data with normal viscosity, $\alpha = 1$, are denoted as (V), data with hyperviscous dissipation $\alpha = 2$ and $\alpha = 4$ are identified through the labels H1 and H2, respectively. We use a pseudospectral code on up to 2048^3 collocation points in a triply periodic domain Ω of size $L = 2\pi$. Full dealiasing is implemented by application of the two-thirds rule [52]. The homogeneous and isotropic external force \mathbf{f} is defined via a second-order Ornstein-Uhlenbeck process in a band of Fourier modes $k \in [0.5, 1.5]$ [36,53]. The resolution of the simulations quantified in terms of the grid spacing dx and the Kolmogorov microscale $\eta_{\alpha} = (\nu^3/\varepsilon)^{1/6\alpha-2}$ [50], where ε is the dissipation rate, is $\eta_{\alpha}/dx \simeq 0.7$ for all simulations.

Each data-set consists of a set of instantaneous velocity fields sampled after the simulations have reached a statistically stationary state. The steady-state energy spectrum $E(k)$ and the dissipation spectrum $k^2E(k)$ obtained by averaging over the sampled data for data-sets V1, V2, H1 and H2 are shown in Figure 1(a,b), respectively. The effects of using hyperviscosity are different if judged on the spectral properties or on the energy flux. Hyperviscous data have a large bottleneck [54] in the high wavenumber range which makes unclear if there is a gain in the scaling range with respect to the viscous case for the same resolution (see Figure 1). On the other hand, the extension of the scaling for the hyperviscous energy flux is more pronounced (see Figure 2).

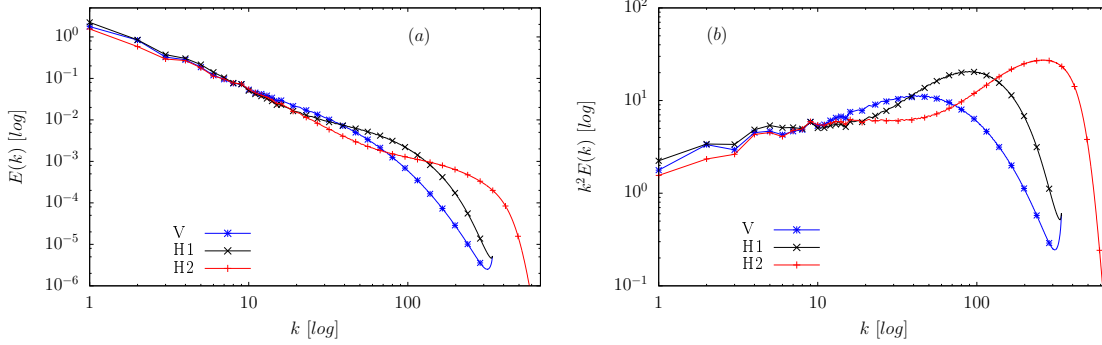


Figure 1. Kinetic energy spectra $E(k)$ (a) and dissipation spectra $k^2 E(k)$ (b) for data-sets V1, V2, H1 and H2. The dissipation spectra $k^2 E(k)$ instead of their hyperviscous counterparts $k^{2\alpha} E(k)$ are shown because the former are connected to the (physical) velocity-field gradients, which are used to estimate a Reynolds number for the hyperviscous simulations in a consistent way compared to run V1 and V2. See also table 1.

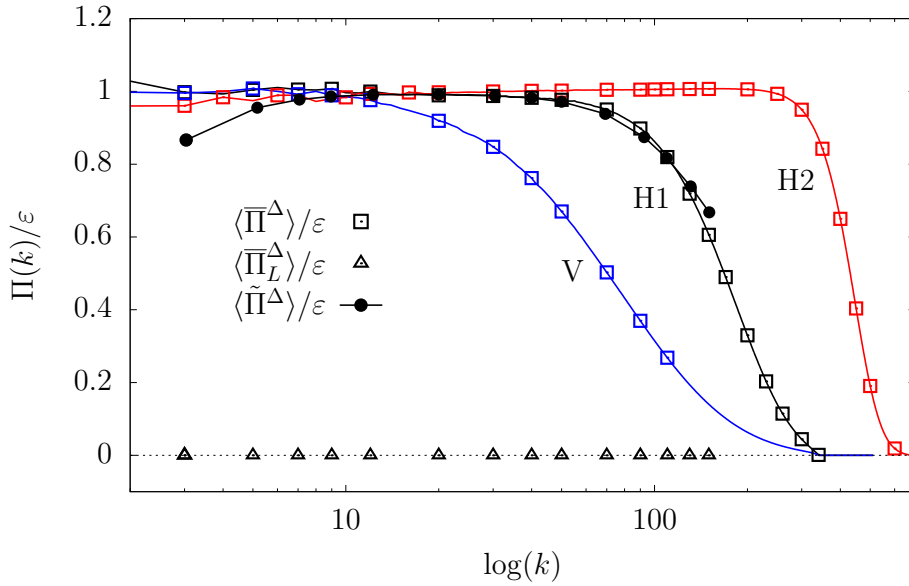


Figure 2. Comparison between the normalised Fourier-space energy flux and the normalised P-SFS (squares) and F-SFS (dots) energy transfers and the Leonard component (triangles) as a function of the cut-off wavenumber $k_c = \pi/\Delta$ for data-sets V1 (blue/dark grey), V2 (green/light grey), H1 (black) and H2 (red/grey). The F-SFS energy transfer for the smooth Gaussian filter is shown for data-set H1 only.

3. Background considerations

As said, in this paper we will focus only on *a priori* analysis of DNSs of isotropic turbulence. The main interest is to have a systematic benchmark of key turbulent statistical properties to validate real applications of LES. In the following, we briefly summarise the main subtleties connected to the definition of filter in LES and on its impact on the multiscale statistics of the sub-grid energy transfer. The governing equations for LES are derived by first applying a filtering operation to the incompressible Navier-Stokes

equations

$$\partial_t \tilde{\mathbf{v}} + \nabla \cdot (\widetilde{\mathbf{v} \otimes \mathbf{v}}) = -\nabla \tilde{p} + \nu \Delta \tilde{\mathbf{v}} \quad (3)$$

where the filtered quantities are defined through a filter G_Δ , and Δ indicates the filter threshold. The filtered velocity field is then given by

$$\tilde{\mathbf{v}}(\mathbf{x}, t) \equiv \int_{\Omega} d\mathbf{y} G_\Delta(|\mathbf{x} - \mathbf{y}|) \mathbf{v}(\mathbf{y}, t) = \sum_{\mathbf{k} \in \mathbb{Z}^3} \hat{G}_\Delta(|\mathbf{k}|) \hat{\mathbf{v}}(\mathbf{k}, t) e^{i\mathbf{k}\mathbf{x}}, \quad (4)$$

with \hat{G}_Δ being the Fourier transform of G_Δ . The aim of LES is to describe the dynamics of the larger scales of the flow, hence the filtering operation given by G_Δ is a ‘coarse-graining’ procedure which removes scales smaller than the given threshold Δ . In this paper, we will use a Gaussian kernel $\hat{G}_\Delta(|\mathbf{k}|) = \exp(-|\mathbf{k}|^2 \Delta^2/2)$. In order to explicitly separate the terms depending on the SFSs, it is useful to introduce the filtered SFS stress tensor (F-SFS). Note that the filtering operation does not produce a clear Fourier spectral distinction between resolved and unresolved scales; hence in this context, the adjective ‘resolved’ is meant to characterise the energy left to the field at each scale after the filtering operation.

$$\tilde{\tau}_{ij}^\Delta(\mathbf{v}, \mathbf{v}) \equiv \widetilde{v_i v_j} - \tilde{v}_i \tilde{v}_j, \quad (\text{F-SFS}) \quad (5)$$

and to rewrite Equation (3) as

$$\partial_t \tilde{\mathbf{v}} + \nabla \cdot (\tilde{\mathbf{v}} \otimes \tilde{\mathbf{v}}) = -\nabla \tilde{p} - \nabla \cdot \tilde{\tau}^\Delta(\mathbf{v}, \mathbf{v}) + \nu \Delta \tilde{\mathbf{v}}. \quad (6)$$

Note that the definition of $\tilde{\tau}_{ij}^\Delta$ comes from the exact application of a low pass filter to each term of the Navier-Stokes equations. So, as long as the unclosed SFS-tensor is known, the filtering procedure is still exact and Equation (6) describes the evolution of a filtered field at all time. In application, the filtering protocol would be useless without the introduction of a closure model for $\tilde{\tau}^\Delta(\mathbf{v}, \mathbf{v})$ in terms of the resolved-scale velocity, i.e. $\tilde{\tau}^\Delta(\mathbf{v}, \mathbf{v}) \rightarrow \tilde{\tau}_{mod}^\Delta(\tilde{\mathbf{v}}, \tilde{\mathbf{v}})$, such that

$$\partial_t \tilde{\mathbf{v}} + \nabla \cdot (\tilde{\mathbf{v}} \otimes \tilde{\mathbf{v}}) = -\nabla \tilde{p} - \nabla \cdot \tilde{\tau}_{mod}^\Delta(\tilde{\mathbf{v}}, \tilde{\mathbf{v}}). \quad (\text{F-LES}) \quad (7)$$

In the following, we will refer to formulation (7) as the ‘Filtered LES’ (F-LES). The solution to Equation (7) leads to a break of the property of being a ‘filtered’ field, because the product of two or more filtered quantities is not the result of the application of a filter and both the advection terms on the left-hand side (LHS) and the closure for the SFS-tensor on the right-hand side (RHS) will introduce uncontrolled errors in any defiltering procedure. More precisely, since the Gaussian filter retains all scales, it is in principle invertible and one could recover the full field from the filtered data. However, replacing the SFS stress tensor with a model breaks this property of the filter and leads to errors in the reconstructed data [2] (note that defiltering can be an ill-conditioned operation). As a result, any practical implementation of (7) will need to evolve the equations on a numerical grid and make sure to introduce some effective numerical dissipation scheme that will remove the energy transferred subgrid. Moreover, the original exact filtered Equation (6) does depend on the shape of the filter, while in (7) we have lost connection with the

original filtering protocol, opening the question about how to validate the closure. In principle, one should reverse-engineer the procedure: given the results of a LES evolution, derive the filter shape that would give the correct agreement if applied to a fully resolved evolution [2]. Still, there are problems to define the set of observables that should be used to follow this procedure.

A natural way to avoid the above complications is to use a filter which is a projector, i.e. a filter that produces the same result when operating multiple times on the same field. In terms of its Fourier expression, a projector filter has the property that: $(\hat{G}_\Delta(|\mathbf{k}|))^2 = \hat{G}_\Delta(|\mathbf{k}|)$ [2]. In what follows, the distinction between projector and non-projector filters is reflected in the notation $\overline{(\cdot)}$ for projected quantities, while $\tilde{(\cdot)}$ is used to indicate the application of a filter which is not a projector. The most common projector widely used in LES for both real and Fourier applications [2,3,17,55,56] is a Galerkin truncation for all wavenumbers larger than a given cut-off wavenumber $k_c = \pi/\Delta$

$$\overline{\mathbf{v}}(\mathbf{x}, t) \equiv \sum_{\mathbf{k} \in \mathbb{Z}^3} \hat{G}_\Delta(|\mathbf{k}|) \hat{\mathbf{v}}(\mathbf{k}, t) e^{i\mathbf{k}\mathbf{x}} = \sum_{|\mathbf{k}| < k_c} \hat{\mathbf{v}}(\mathbf{k}, t) e^{i\mathbf{k}\mathbf{x}} . \quad (8)$$

In order to define the evolution of $\overline{\mathbf{v}}(\mathbf{x}, t)$ properly, i.e. such that it is confined to the same finite-dimensional vector space, we need to project the non-linear term of Equation (6), resulting in

$$\partial_t \overline{\mathbf{v}} + \nabla \cdot (\overline{\mathbf{v}} \otimes \overline{\mathbf{v}}) = -\nabla \overline{p} - \nabla \cdot \overline{\tau}^\Delta(\mathbf{v}, \mathbf{v}) + \nu \Delta \overline{\mathbf{v}} . \quad (9)$$

In Equation (9), the projected SFS stress tensor (P-SFS) is now given by

$$\overline{\tau}_{ij}^\Delta(\mathbf{v}, \mathbf{v}) = \overline{v_i v_j} - \overline{v_i} \overline{v_j} , \quad (\text{P-SFS}) . \quad (10)$$

Again, in real *a posteriori* [19] implementations, the P-SFS stress tensor in Equation (10) should be replaced by a model, i.e. $\overline{\tau}^\Delta(\mathbf{v}, \mathbf{v}) \rightarrow \overline{\tau}_{mod}^\Delta(\overline{\mathbf{v}}, \overline{\mathbf{v}})$, and one obtains

$$\partial_t \overline{\mathbf{v}} + \nabla \cdot (\overline{\mathbf{v}} \otimes \overline{\mathbf{v}}) = -\nabla \overline{p} - \nabla \cdot \overline{\tau}_{mod}^\Delta(\overline{\mathbf{v}}, \overline{\mathbf{v}}) , \quad (\text{P-LES}) \quad (11)$$

which in the following is referred to as ‘Projected LES’ (P-LES). Notice that we now have a consistent definition of the ‘filtering’ protocol and we should have called the unclosed tensor in (10) ‘subgrid-scales’ (SGS) differentiating it from the one called ‘subfilter-scales’ (SFS) in (6) as it can be found in previous literature [20,57,58]. The difference originates from the fact that the Galerkin truncation removes all Fourier modes below the cut-off scale, while a non-projector filter does not necessarily do so. Hence, unlike for a non-projector filter, for a Galerkin projector there is an exact correspondence between the finest LES grid scale and the cut-off scale. Keeping in mind the above difference, in our *a-priori* analyses, the velocity fields are always evolved by fully resolved DNS, inconsistent with the concept of a-posteriori LES on a specified grid. For this reason, we have simplified the notation in F-SFS and P-SFS which allows us to give emphasis to the filters’ properties.

In formulation (11), the inertial term is also a projected function, and the evolution of $\overline{\mathbf{v}}(\mathbf{x}, t)$ is confined to a manifold whose dimension is specified by the chosen threshold k_c (see the following for other possible definitions of non-sharp Fourier-projectors). It may be worth mentioning that, in mathematical analysis, one can use a sequence of

decreasing filter scales of a Galerkin projector to converge to a weak solution of the Navier Stokes equations along a subsequence [59]. It is important to realise that one might have used a formulation like Equations (10) and (9) for filters which are not projectors. This would not solve the dichotomy among filter-scale and grid-spacing and, more importantly, double filtering the inertial term with a non-projector filter breaks the Galilean invariance of the corresponding SFS stress tensor as shown in Appendix A.1. Using a P-LES has also the advantage (in principle) that the shape of the filter explicitly appears in the space time evolution, because of the need to further project the non-linear term (and the modelled SFS tensor) at each time step in (9). In practice, any numerical implementation of both F-LES or P-LES, requires a dynamical projection on a finite grid which takes into account also the possible aliasing errors. Such a further projection needs always to be applied in the implementation of the F-LES system. For the P-LES system, the projector in front of the non-linear term includes already a dealiasing operation if the filter cut-off wavenumber is smaller than $2/3k_{max}$, where k_{max} is the largest resolved wavenumber. In any case, aliasing error does not play a role in the *a priori* data analysis carried out here, since all data were obtained from fully dealiased DNS. This means that the F-LES (6) should be seen as ‘mathematical LES’ and not practical for a-posteriori LES implementations on finite grids [57]. The choice of the smooth filter used in our F-LES ensures a high level of filtering after the cut-off scale, implying that the effect of a further projection on the grid would be negligible. This is possible because we considered only the a-priori analysis. In any practical LES implementations, an additional projection on the LES grid and an SGS model with dissipation to maintain stability are needed, even in case of strong filtering. The main mathematical advantage of considering smooth filters is that the SFS stress tensor is positive definite. As a consequence, they can be applied in the derivation of scaling properties of the physical space velocity field [47].

3.1. *A priori definition of the energy transfer using the F-SFS or P-SFS formulations*

A key benchmark quantity to validate the accuracy of a LES is the ability to reproduce the correct mean and fluctuating properties of the SFS energy transfer. In the smooth filtering approach, where no projectors are applied to the equations, the resolved kinetic energy evolves according to

$$\frac{1}{2}\partial_t(\tilde{v}_i\tilde{v}_i) + \partial_j B_j = -\tilde{\Pi}^\Delta \quad (12)$$

where $B_j = \tilde{v}_j \frac{\tilde{v}_i \tilde{v}_i}{2} + \tilde{v}_i(\tilde{p}\delta_{ij} + \tilde{\tau}_{ij}^\Delta)$ is a spatial transport term that redistributes the resolved energy among different spatial positions while

$$\tilde{\Pi}^\Delta = -\tilde{\tau}_{ij}^\Delta(\partial_j \tilde{v}_i) = -\tilde{\tau}_{ij}^\Delta \tilde{s}_{ij} \ , \quad (13)$$

is the instantaneous SFS energy flux, where $\tilde{s}_{ij} = (\partial_i \tilde{v}_j + \partial_j \tilde{v}_i)/2$ denotes the resolved strain-rate tensor. In the formulation based on a projector filter, the local resolved kinetic energy evolves differently, since from Equation (9) we obtain the following evolution equation for the resolved kinetic energy:

$$\frac{1}{2}\partial_t(\bar{v}_i\bar{v}_i) = -\bar{v}_i\overline{\bar{v}_j\partial_j\bar{v}_i} - \bar{v}_i\partial_j\bar{p}\delta_{ij} - \bar{v}_i\partial_j\bar{\tau}_{ij}^\Delta \ , \quad (14)$$

where the first term on the RHS is no longer a total derivative, since

$$\overline{v_i \overline{v_j} \partial_j \overline{v_i}} = \partial_j (\overline{v_i \overline{v_j} \overline{v_i}}) - (\partial_j \overline{v_i}) (\overline{v_j \overline{v_i}}) . \quad (15)$$

The equation for the SFS energy transfer therefore becomes

$$\frac{1}{2} \partial_t (\overline{v_i \overline{v_i}}) + \partial_j A_j = -\overline{\Pi}^\Delta + (\partial_j \overline{v_i}) (\overline{v_j \overline{v_i}}) \quad (16)$$

with $A_j = \overline{v_i} (\overline{v_i \overline{v_j}} + \overline{p} \delta_{ij} + \overline{\tau}_{ij}^\Delta)$ as the flux term. Now, the RHS of Equation (16) consists of the P-SFS tensor

$$\overline{\Pi}^\Delta = -\overline{\tau}_{ij}^\Delta \overline{s}_{ij} , \quad (17)$$

and the additional term

$$\overline{\pi}^\Delta = (\partial_j \overline{v_i}) (\overline{v_j \overline{v_i}}) \quad (18)$$

which is not Galilean invariant. Note that in Equations (12), (14) and (16) we have not explicitly written, for the sake of simplicity, the viscous contributions. We will omit the viscous terms in the remainder of this paper.

The lack of Galilean invariance of $\overline{\pi}^\Delta$ does not break the *global* Galilean invariance of Equation (16) because of cancellations with terms on the LHS (see Appendix A). Nevertheless, it is clear that adopting this formulation, the total SFS energy transfer using the P-SFS stress tensor:

$$\mathcal{P}^\Delta = -\overline{\Pi}^\Delta + \overline{\pi}^\Delta = -(\partial_i \overline{v_j}) \overline{v_i \overline{v_j}} \quad (19)$$

is not pointwise Galilean invariant. The non-Galilean invariant term, $\overline{\pi}^\Delta$, is closed in terms of the resolved fields and must not be considered a true SFS transfer. Indeed, it is easy to realise that its mean value over the whole volume is always vanishing:

$$\langle \overline{\pi}^\Delta \rangle = \frac{1}{|\Omega|} \int_{\Omega} d\mathbf{x} (\partial_j \overline{v_i}) \overline{v_j \overline{v_i}} = 0 , \quad (20)$$

where we have used the filter property $\langle \overline{f \overline{g}} \rangle = \langle \overline{f g} \rangle$, the projector property $G^2 = G$ and incompressibility to write $(\partial_j \overline{v_i}) \overline{v_j \overline{v_i}}$ as a total derivative. The net SFS energy transfer \mathcal{P}^Δ consists of genuine SGS coupling term $\overline{\Pi}^\Delta$ and a contribution $\overline{\pi}^\Delta$ due to self-coupling of the resolved scales which breaks pointwise Galilean invariance. The pointwise lack of Galilean invariance of the ‘unsubtracted flux’ results in unphysical large fluctuations as shown in [49] which might lead to different multiscale results compared to those of $\overline{\Pi}^\Delta$ and $\tilde{\Pi}^\Delta$ (see Section 4.2).

The lack of Galilean invariance can be solved by exploiting the freedom to add and subtract a term that will make both the RHS and the LHS separately Galilean invariant. In particular, we rewrite the energy balance as

$$\frac{1}{2} \partial_t (\overline{v_i \overline{v_i}}) + \partial_j A_j = -\overline{\Pi} + (\partial_j \overline{v_i}) \tau_{ij}^{\Delta,L} + \frac{1}{2} \partial_j (\overline{v_j \overline{v_i} \overline{v_i}}) , \quad (21)$$

ID	Stress tensors	Energy transfers
F-SFS	$\tilde{\tau}_{ij}^\Delta = \overline{v_i v_j} - \tilde{v}_i \tilde{v}_j$	$\tilde{\Pi} = -\tilde{s}_{ij} \tilde{\tau}_{ij}^\Delta$
P-SFS	$\bar{\tau}_{ij}^\Delta = \overline{v_i v_j} - \bar{v}_i \bar{v}_j$	$\bar{\Pi} = -\bar{s}_{ij} \bar{\tau}_{ij}^\Delta$
P-SFS(nG)	$\bar{\tau}_{ij}^\Delta = \overline{v_i v_j} - \bar{v}_i \bar{v}_j$	$\mathcal{P}^\Delta = -\bar{s}_{ij} \bar{v}_i \bar{v}_j$
Leonard	$\tau_{ij}^{\Delta,L} = \overline{v_i v_j} - \bar{v}_i \bar{v}_j$	$\bar{\Pi}_L^\Delta = -\bar{s}_{ij} \tau_{ij}^{\Delta,L}$

Table 2. Summary of definitions of stresses and instantaneous energy transfers. The label nG indicates that the corresponding SFS energy transfer is not Galilean invariant.

where we have introduced the Leonard stress [60], $\tau_{ij}^{\Delta,L}$:

$$\tau_{ij}^{\Delta,L} \equiv \overline{v_i v_j} - \bar{v}_i \bar{v}_j, \quad (22)$$

plus another term which is a total derivative and that can be moved to the LHS of Equation (16). Hence, the kinetic energy balance based on the P-SFS stress tensor becomes

$$\frac{1}{2} \partial_t (\bar{v}_i \bar{v}_i) + \partial_j \left(A_{ij} - \frac{1}{2} \bar{v}_i \bar{v}_i \bar{v}_j \right) = -\bar{\Pi}^\Delta - \bar{\Pi}_L^\Delta, \quad (23)$$

where $\bar{\Pi}_L^\Delta = -\tau_{ij}^{\Delta,L} \bar{s}_{ij}$ is the energy transfer corresponding to the Leonard stress. The RHS and LHS of Equation (23) are now separately Galilean invariant, and we have a way to assess the properties of the energy balance without being affected by spurious effects. The introduction of the Leonard stress tensor has been also used in the literature to preserve Galilean invariance in the definition of models for a-posteriori LES [61]. The transfer involving SFS quantities is given by $\bar{\Pi}^\Delta$ alone because the Leonard stress describes only a coupling among resolved scales and its contribution to the mean SFS energy transfer vanishes when averaged on the whole volume. In Figure 3, we show the joint probability density function (pdf) of the two contributions to the total SFS energy transfer for a typical cut-off in the inertial range, $k_c = 20$, from where it is clear that $\bar{\Pi}^\Delta$ and $\bar{\Pi}_L^\Delta$ are nearly uncorrelated.

In summary, the use of a projector to define the filtering operation results in a sharp distinction between two SFS energy transfer contributions, one described by a genuine correlation among resolved and SFSs, $\bar{\Pi}^\Delta$, and another one due to a self-coupling of the resolved scales, $\bar{\Pi}_L^\Delta$. On the other hand, the total F-SFS energy transfer $\tilde{\Pi}^\Delta$ contains local contributions which are not strictly associated with the SFSs, since it has the same formal structure as $\bar{\Pi}^\Delta + \bar{\Pi}_L^\Delta$. Only the global average on the whole volume of the SFS energy transfer is correctly described by the F-SFS approach, while its local values $\tilde{\Pi}^\Delta$ are affected by contributions coming from self-coupling of the resolved scales. A summary of all definitions of SFS stresses and energy transfers is given in Table 2.

4. Anomalous scaling properties of the SFS energy transfer

In order to build models which are able to describe higher-order statistical features of a turbulent flow, it is important to distinguish physically relevant fluctuations from unphysical fluctuations. Unphysical fluctuations can be induced by the filter, e.g. a

sharp Galerkin projector is discontinuous in Fourier space and therefore induces Gibbs oscillations in physical space, which can contaminate the measured statistical signal [62]. Fluctuations can also originate from the residual self-coupling of the resolved scales and from a lack of Galilean invariance of the SFS energy transfer, as discussed in further detail in the coming section. Obtaining a clear statistical signature of the SFS energy transfer fluctuations is especially important for the assessment of backscatter contributions. It is known that the pdf of $\tilde{\Pi}^\Delta$ obtained using a smooth Gaussian filter has large tails skewed toward the positive values, in agreement with the existence of a direct energy cascade both in mean and for local intense events [17,44].

4.1. Mean properties

Figure 2 shows a comparison between the total flux across a spherical shell of radius k_c in Fourier-space,

$$\Pi(k_c) = \sum_{k'=1}^{k_c} \sum_{|\mathbf{k}|=k'} ik_j \hat{u}_i(\mathbf{k})^* \sum_{\mathbf{p} \in \mathbb{Z}^3} \hat{u}_i(\mathbf{p}) \hat{u}_j(\mathbf{k} - \mathbf{p}), \quad (24)$$

and the different contributions to the SFS energy transfer for a sharp projector $\langle \bar{\Pi}^\Delta \rangle$ and $\langle \bar{\Pi}_L^\Delta \rangle$ as a function of the cut-off wavenumber $k_c = \pi/\Delta$ and for different Reynolds numbers. As expected, the contribution originating from the Leonard stress vanishes, $\langle \bar{\Pi}_L^\Delta \rangle = 0$, while the Fourier flux is exactly reproduced by $\langle \bar{\Pi}^\Delta \rangle$ due to the Parseval identity. Here and hereafter we adopt the notation $\langle \cdot \rangle$ to indicate an average over the entire physical volume. For comparison, we also show the mean SFS energy transfer obtained from the Gaussian filter as a function of $k_c = \pi/\Delta$. The latter does not match exactly the Fourier-space energy flux at small filter thresholds, indicating non-trivial coupling among degrees of freedoms above and below the filter width. Deviations between $\langle \tilde{\Pi}^\Delta \rangle$ and $\Pi(k)$ can indeed be expected, since the $\langle \tilde{\Pi}^\Delta \rangle$ can be expressed as weighted average in Fourier-space centred around $k_c = \pi/\Delta$ [47,63], and there is no *a priori* reason for $\Pi(k)$ to match its weighted average.

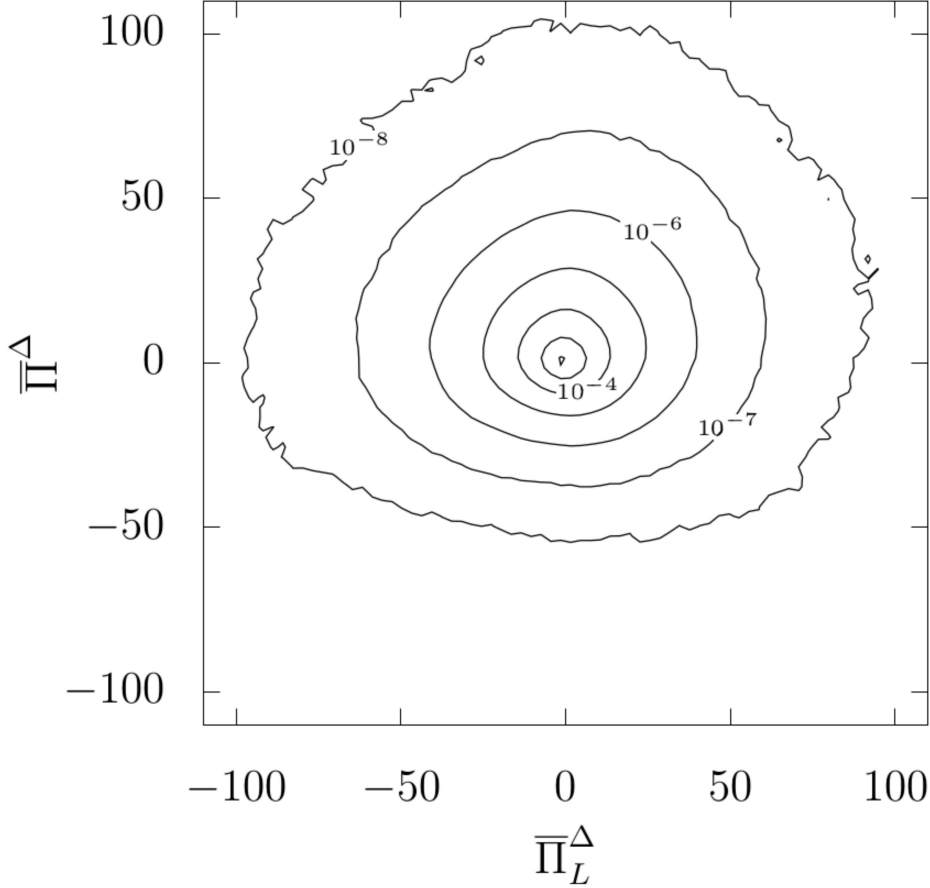


Figure 3. Joint pdf of the P-SFS energy transfer and the Leonard component for a sharp projector at cut-off wavenumber $k_c = 20$ from data-set H1.

4.2. *Effects of non-Galilean invariance*

According to Equation (16), the non-Galilean invariant definition of the P-SFS energy transfer \mathcal{P}^Δ consists of two terms: $\bar{\Pi}^\Delta$, which is Galilean invariant and couples the resolved and the unresolved scales and the non-Galilean invariant $\bar{\pi}^\Delta$, which is given only in terms of the resolved fields. In Figure 4, we show the effects of breaking Galilean invariance by comparing the pdf of the different contributions and of the ones obtained by introducing the Leonard stress and therefore recovering the invariance term by term. As one can see, the fluctuations of the ‘unsubtracted flux’ \mathcal{P}^Δ are much larger than those of the invariant terms, confirming the importance of Galilean invariance [48,49]. In order to quantify the difference between the fluctuations of \mathcal{P}^Δ and the other components of the P-SFS energy transfer, we also show the standard deviations of all components. In Figure 4(b), we show that the non-Galilean invariant definition of the P-SFS energy transfer \mathcal{P}^Δ is between one and three orders of magnitude larger than those corresponding to the other terms.

Since the fluctuations of $\bar{\Pi}^\Delta$ are orders of magnitude smaller than the fluctuations of $\mathcal{P}^\Delta = \bar{\Pi}^\Delta + \bar{\pi}^\Delta$, the large tails of the latter must be connected to $\bar{\pi}^\Delta$. The question now arises whether these large spurious fluctuations originate from a lack of Galilean invariance or if they are due to the self-coupling among the resolved scales. The latter can be quantified through the fluctuations of the component of the Leonard

stress, $\overline{\Pi}_L^\Delta$. As shown by Figure 4(a,b), both $\overline{\Pi}^\Delta$ and $\overline{\Pi}_L^\Delta$ have similar fluctuations. We therefore conclude that a lack of Galilean invariance has a drastic effect on the fluctuations of the SFS energy transfer and that it becomes larger and larger by decreasing the cut-off scale.

The properties of the non-Galilean invariant ‘unsubtracted flux’ \mathcal{P}^Δ obtained from a sharp spectral projector were discussed in Ref. [49] also in the context of locality of the energy cascade. Unlike $\overline{\Pi}^\Delta + \overline{\Pi}_L^\Delta$, which was rigorously proven to be pointwise scale-local as non-local contributions from sweeping effects were removed, \mathcal{P}^Δ only becomes scale-local in an average sense since the sweeping contributions cancel under space averaging. We conclude that potential spurious fluctuations introduced by a lack of Galilean invariance may be of concern in LES, and the unsubtracted flux \mathcal{P}^Δ will not be considered further in this paper.

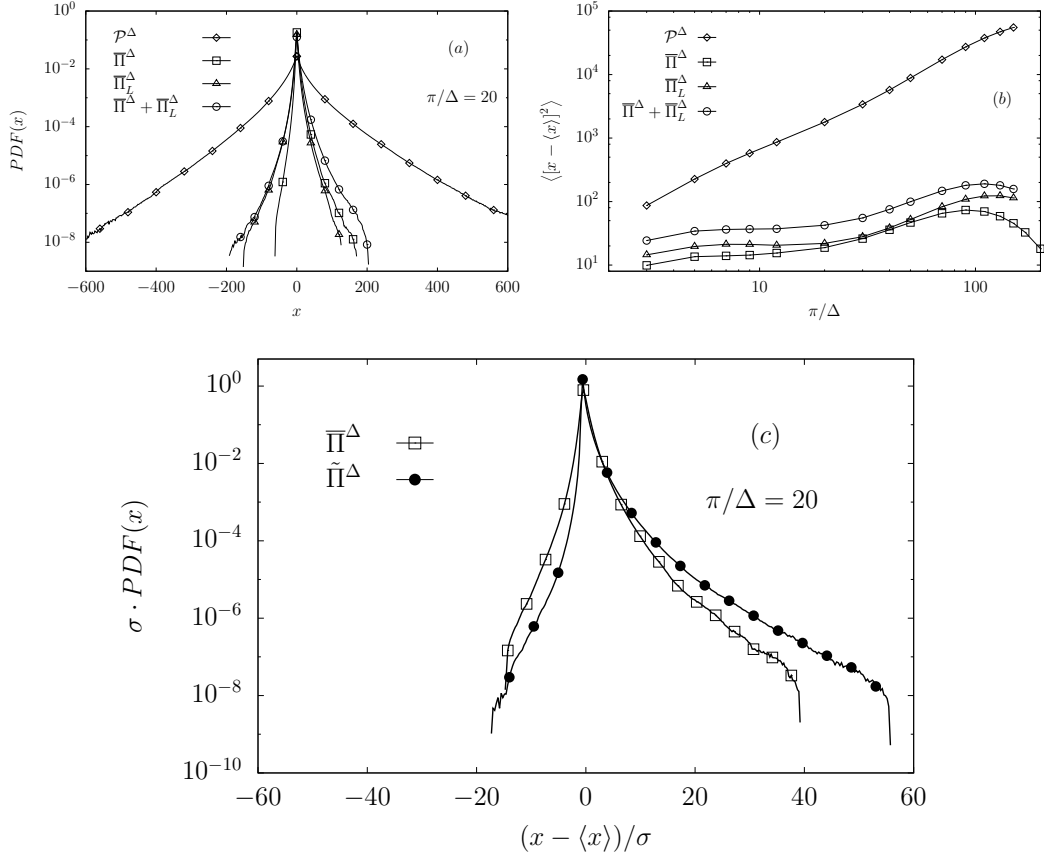


Figure 4. (a) The pdfs of different components of the P-SFS energy transfer. (b) Standard deviation of the corresponding pdfs as a function of the cut-off wavenumber π/Δ . (c) Comparison between the standardised pdfs of the P-SFS energy transfer for a sharp projector and of the F-SFS energy transfer for a smooth Gaussian filter at $\Delta = \pi/20$. Data are taken from data-set H1.

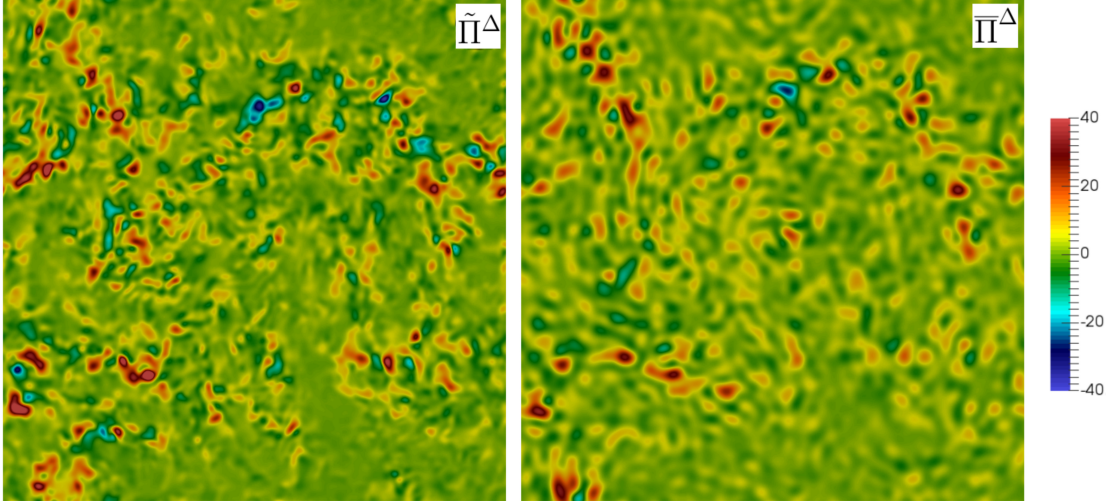


Figure 5. Visualisations of the SFS energy transfer in a plane cut through the volume. Positive values indicate forward energy transfer, while negative values correspond to backscatter. Left: F-SFS (Gaussian filter), right: P-SFS (sharp spectral projector) at $k_c = \pi/\Delta = 20$ for data-set H1.

In Figure 4(c), we show the normalised pdfs of $\tilde{\Pi}^\Delta$ and $\bar{\Pi}^\Delta$ at comparable filter thresholds. Hence, both the Gaussian filter and the real subfilter component of the sharp projector have a statistical signal correlated with the global forward energy cascade mechanism. This is apparently not the case for the other components of the SFS energy transfer obtained from a sharp projector, since the pdfs of $\bar{\Pi}^\Delta + \bar{\Pi}_L^\Delta$ and $\bar{\Pi}_L^\Delta$ shown in Figure 4(a) are more symmetric than the pdf of $\bar{\Pi}^\Delta$. Since $\bar{\Pi}_L^\Delta$ describes the energy transfers among the resolved scales which vanish on average, the negative tail in $\bar{\Pi}_L^\Delta$ and therefore to some extent also the negative tail in $\bar{\Pi}^\Delta + \bar{\Pi}_L^\Delta$ cannot be a genuine backscatter signal. In summary, the above results further support the role of $\bar{\Pi}^\Delta$ as the most relevant component of the P-SFS energy transfer. Figure 5 shows visualisations of the P-SFS energy transfer $\bar{\Pi}^\Delta$ and the F-SFS energy transfer $\tilde{\Pi}^\Delta$ for data-set H1 obtained by a plane cut through the volume. The filter thresholds for $\bar{\Pi}^\Delta$ and $\tilde{\Pi}^\Delta$ are the same as that of their pdfs shown in Figure 4(c). The data corresponding to the F-SFS energy transfer resolve slightly smaller structures compared to the P-SFS data, which can be expected as Gaussian smoothing does not result in a reduction of the degrees of freedom in the same way Galerkin truncation does.

4.3. Intermittency and anomalous scaling

An accurate LES should reproduce the correct multiscale properties of the SFS stress tensor and energy transfer. It is well known that turbulence contains anomalous scaling (intermittency) in the inertial range of scales [1]. Intermittency is typically measured through the scaling properties of high-order moments of the velocity increments as a function of the separation scale or in terms of moments of velocity gradients as a function of Reynolds number. More precisely, the longitudinal and transverse velocity increments are defined as $\delta v_L(\mathbf{x}, \mathbf{r}) \equiv \delta \mathbf{v}(\mathbf{x}, \mathbf{r}) \cdot \hat{\mathbf{r}}$ and $\delta \mathbf{v}_T(\mathbf{x}, \mathbf{r}) \equiv \delta \mathbf{v}(\mathbf{x}, \mathbf{r}) - \delta v_L(\mathbf{x}, \mathbf{r}) \hat{\mathbf{r}}$ respectively, where $\delta \mathbf{v}(\mathbf{x}, \mathbf{r}) \equiv \mathbf{v}(\mathbf{x} + \mathbf{r}) - \mathbf{v}(\mathbf{x})$ is the two-point velocity difference at separation vector \mathbf{r} and $\hat{\mathbf{r}}$ is the unit vector along \mathbf{r} . The n^{th} -order moments of $\delta v_L(\mathbf{x}, \mathbf{r})$

and $\delta\mathbf{v}_T(\mathbf{x}, \mathbf{r})$ are the longitudinal structure function (LSF) and the transverse structure function (TSF),

$$S_L^{(n)}(r) \equiv \langle (\delta v_L(\mathbf{x}, \mathbf{r}))^n \rangle, \quad S_T^{(n)}(r) \equiv \langle |\delta\mathbf{v}_T(\mathbf{x}, \mathbf{r})|^n \rangle, \quad (25)$$

respectively, where $\langle \cdot \rangle$ denotes space and time averages and we have assumed isotropy for simplicity. At high Reynolds numbers both the LSF and TSF show inertial-range anomalous scaling:

$$S_L^{(n)}(r) \sim r^{\zeta_L(n)} \quad S_T^{(n)}(r) \sim r^{\zeta_T(n)} \quad (26)$$

with scaling exponents that are multifractal [1] and different from the Kolmogorov prediction $n/3$. We differentiate between longitudinal and transverse exponents because empirical measurements show a small difference between the two sets (see [64] for a recent discussion on the Reynolds number dependency of the mismatch among longitudinal and transverse scaling exponents and [65] for theoretical considerations). A typical signature of intermittency is given by the growth of the flatness:

$$F_{L,T}(r) = \frac{S_{L,T}^{(4)}(r)}{(S_{L,T}^{(2)}(r))^2} \sim r^{\zeta_{L,T}(4) - 2\zeta_{L,T}(2)}. \quad (27)$$

Because $F_{L,T} = 3$ for Gaussian distributions, the empirical observation that $\zeta(4) \neq 2\zeta(2)$ quantifies the departure from Gaussian statistics. More importantly, such non-Gaussian fluctuations are present even at relatively small Reynolds numbers [45,46,66]. As a result, the problem of validating any SFS model beyond second-order (spectral) properties is important, both for applications and fundamental studies.

Of interest is the connection between the scaling properties of the SFS energy transfer as a function of the cut-off Δ and the scalings of the LSF and TSF as a function of the increment r . One approach is to treat the filter as a local operation in scale space and to relate the SFS energy transfer at Δ to the corresponding dimensional equivalent in terms of velocity increments at scale $r = \Delta$: $\tilde{\Pi}^\Delta \sim (\delta_\Delta v)^3/\Delta$. Indeed, at a given filter scale, the SFS-stress tensors $\tilde{\tau}^\Delta$ and $\tilde{\bar{\tau}}^\Delta$ can be expressed in terms of averages over velocity field increments at scales less than Δ [67–69]

$$\tilde{\tau}_{ij}^\Delta(\mathbf{x}) = \langle \delta_{\mathbf{r}} v_i(\mathbf{x}) \delta_{\mathbf{r}} v_j(\mathbf{x}) \rangle_\Delta - \langle \delta_{\mathbf{r}} v_i(\mathbf{x}) \rangle_\Delta \langle \delta_{\mathbf{r}} v_j(\mathbf{x}) \rangle_\Delta, \quad (28)$$

where $\langle f \rangle_\Delta = \int d\mathbf{r} f(\mathbf{r}) G_\Delta(\mathbf{r})$ denotes a weighted average over the displacement \mathbf{r} . The same expression holds for $\tilde{\bar{\tau}}^\Delta$. For Hölder-continuous velocity fields with Hölder-exponent h , i.e. if $|\delta_{\mathbf{r}} \mathbf{v}(\mathbf{x})| = O(|\mathbf{r}|^h)$, the following *pointwise* upper bound can be derived for the SFS-energy transfer [68]:

$$\tilde{\Pi}^\Delta = O(\Delta^{3h-1}), \quad (29)$$

provided the filter and its gradient are bounded and decrease sufficiently rapidly at infinity. In order to account for the existence of a multifractal scaling with different local Hölder exponents, the same approach leads to a *global* upper bound and hence a scaling estimate

$$\langle |\tilde{\Pi}^\Delta|^n \rangle = O(\Delta^{\zeta_{3n-n}}), \quad (30)$$

where ζ_n are the anomalous exponents of the n^{th} -order structure functions [47] and where we have neglected the small empirically observed mismatch between longitudinal and transverse increments (which cannot be captured by the above estimate). As for the local upper bound given by inequality (29), the derivation of the rigorous global scaling result presented in Ref. [47] requires conditions on the filter functions which are not satisfied by generic projector filters. However, as we explain in Appendix B, Eyink’s [47] scaling estimates (and upper bounds) can also be shown to apply to our P-SFS energy transfer in Equation (17), if we use a smooth filter. Such a smooth filter can be chosen to approximate a Galerkin projector with arbitrary accuracy at the expense of the upper bound becoming arbitrarily large. To supplement this, we show the scaling of the P-SFS flux in Figure 6 using a sharp Galerkin projector, which agrees with the scaling in Equation (30), even though the rigorous upper bound that can be obtained formally diverges for such a filter. This indicates that the upper bound becomes less useful (less tight) even though the P-SFS flux still scales as the F-SFS, that uses a smooth filter.

The intermittent scaling of the SFS energy transfer was first investigated in *a-priori* as well as *a-posteriori* analyses in Ref. [44] at moderate Reynolds numbers using both a Gaussian filter and a sharp cut-off in Fourier space, but without applying the double filtering proposed here (10). By using ESS [45,46], it was shown in [44] that the scaling of the SFS energy transfer is slightly more intermittent than the LSFs while being less intermittent than the TSFs. However, as pointed out in Ref. [44], the accuracy of the measurements was not sufficient to warrant interpretation of the small differences in the exponents.

In what follows, we intend to perform a similar analysis at much higher Reynolds numbers, such as to avoid the use of ESS, and by comparing different filtering strategies and by analysing different components of the SFS energy transfer.

Figures 6 (a-c) presents the scaling of the SFS energy transfer compared to the predictions from Equation (30) for the different components of the P-SFS energy transfer obtained through Galerkin truncation. and for the F-SFS energy transfer. In all figures we superpose the multifractal prediction using either the longitudinal or the transverse scaling. Indeed, the SFS energy transfer is a scalar quantity that cannot distinguish among the two scalings and one has to interpret the mismatch between the two sets of exponents as an estimate of the error in the scaling properties of mixed observables. From Figure 6 it can be seen that the scaling of all components is consistent with Equation (30) for $n = 2, 3$ and $n = 4$. The Leonard component $\langle (\overline{\Pi}_L^\Delta)^n \rangle$ also scales in agreement with Equation (30) for the even orders $n = 2, 4$ as can be seen in Figures 6 (a) and (c). The odd order $n = 3$ is in very small agreement with the symmetry in the pdf already discussed.

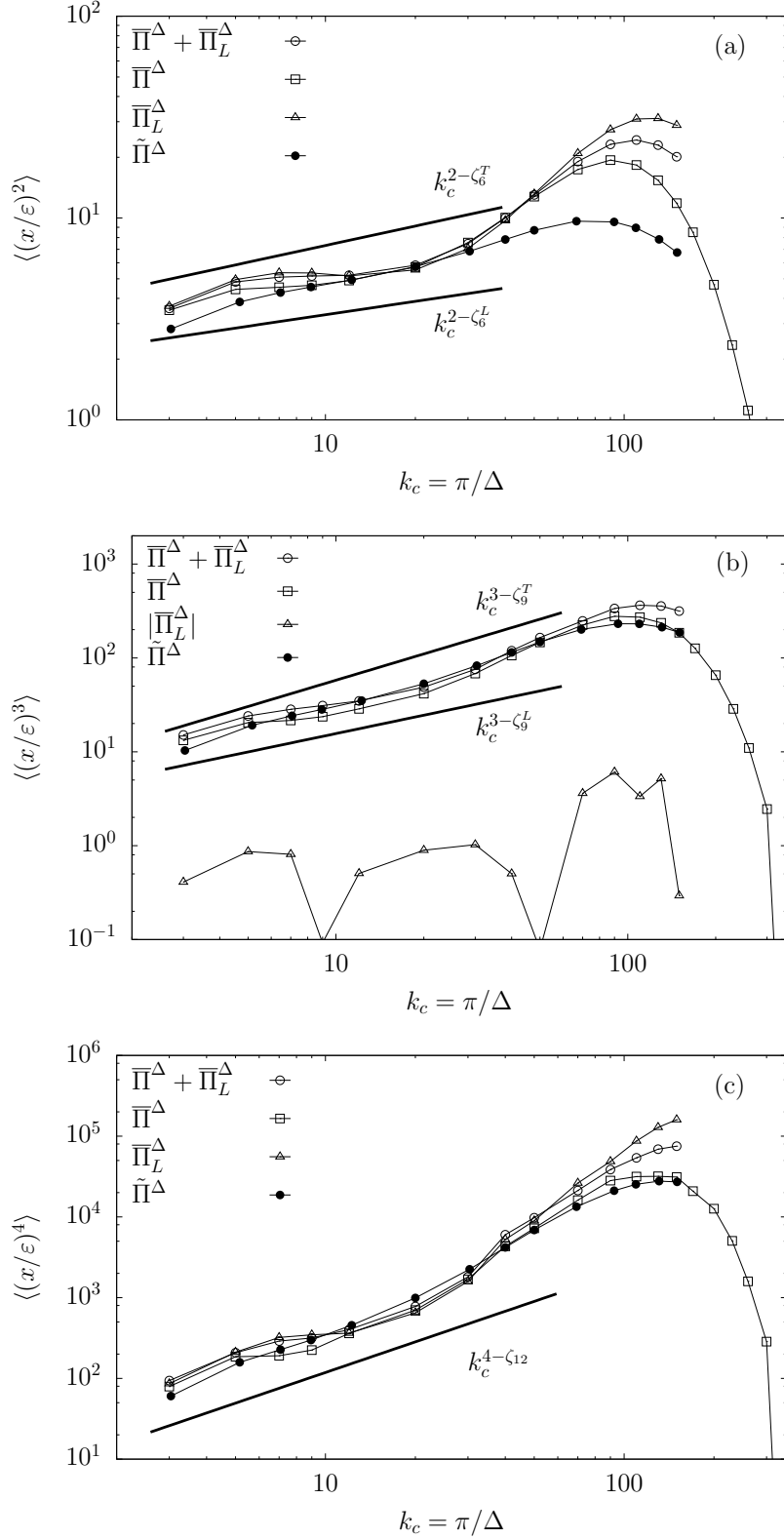


Figure 6. data-set H1. Scaling of the n^{th} moments of the different components of P-SFS and F-SFS energy transfers: (a) $n = 2$, (b) $n = 3$, (c) $n = 4$. The solid lines indicate the scaling expected from the multifractal model and Equation (30) using the anomalous exponents for the longitudinal and transverse structure functions ζ_{3n}^L and ζ_{3n}^T Ref. [6]. In (c), for $n = 4$, the solid line indicates the prediction from the She Lévêque model $\zeta_{3n} = 2.74$ [70,71] is shown. The data corresponding to $\bar{\Pi}^\Delta + \bar{\Pi}_L^\Delta$ and $\tilde{\Pi}^\Delta$ have been shifted for presentational reasons.

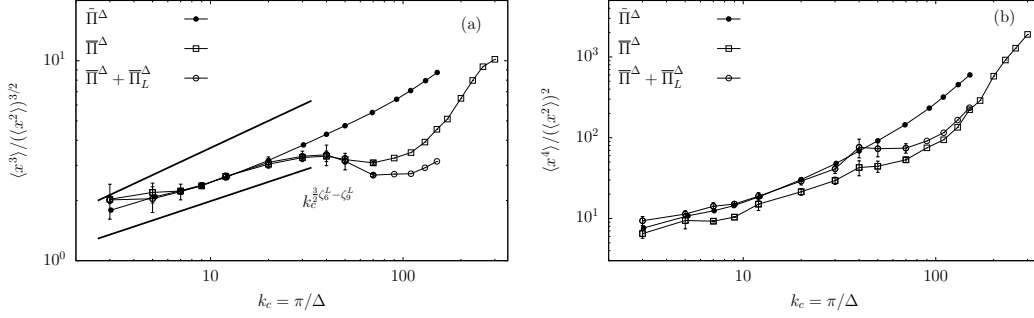


Figure 7. Skewness (a) and flatness (b) of the different components of P-SFS and F-SFS energy transfer for data-set H1. The solid lines in (a) indicate the scaling expected from the multifractal model and Equation (30) using the anomalous exponents for the longitudinal and transverse structure functions ζ_{3n}^L and ζ_{3n}^T , Ref. [6]. The data corresponding to $\bar{\Pi}^\Delta + \bar{\Pi}_L^\Delta$ and $\tilde{\Pi}^\Delta$ have been shifted upward and downward, respectively, for presentational reasons.

Figure 7 shows the skewness and flatness of the P-SFS energy transfer $\bar{\Pi}^\Delta$, its combination with the energy transfer due to the Leonard stresses $\bar{\Pi}^\Delta + \bar{\Pi}_L^\Delta$ and the F-SFS energy transfer $\tilde{\Pi}^\Delta$ obtained through Gaussian filtering. Both skewness and flatness show similar scaling for $\bar{\Pi}^\Delta$, $\bar{\Pi}^\Delta + \bar{\Pi}_L^\Delta$ and $\tilde{\Pi}^\Delta$, however, the scaling range of the skewness corresponding to the F-SFS $\tilde{\Pi}^\Delta$ has a smoother transition when crossing the viscous scales compared to that obtained by sharp Galerkin projection. This is an indication of the importance of contributions from a wide range of scales affecting the F-LES formalism. In other words, since the smooth Gaussian filter is less localised in k -space compared to the sharp projector, it retains contributions from a larger number of Fourier modes at different wavenumbers, see also [63] for an illustration. Concerning the flatness, there appears to be little difference between $\bar{\Pi}^\Delta + \bar{\Pi}_L^\Delta$ and $\bar{\Pi}^\Delta$; the two corresponding curves for the flatness nearly collapse in the intermittent scaling range without any shift in the data.

In summary, the second, third and fourth-order moments as well as the skewness and flatness of the SFS energy transfer for the sharp filter show intermittent scaling for both $\bar{\Pi}^\Delta + \bar{\Pi}_L^\Delta$ and for the P-SFS definition $\bar{\Pi}^\Delta$ alone, in agreement with the local-estimates based on the bridge relation among the SFS energy transfer at filter width Δ and velocity increments at scale $r \sim \Delta$.

4.3.1. Reynolds number dependency

In the remainder of this section, we assess the results for $\bar{\Pi}^\Delta$ by extending the analysis to both a larger and smaller inertial range using the three additional data-sets V1, V2 and H2 described in table 1. Results for the scaling of $\langle (\bar{\Pi}^\Delta)^n \rangle$, obtained from data-sets H1, H2 and V1, V2 are presented in Figures 8(a-c) for $n = 2, 3$ and $n = 4$, respectively. In Figure 8(a) we observe that the intermittent scaling extends to a larger range of scales for the higher Reynolds number data-set H2 and to a shorter range for data-set V1. We note that the effect of the bottleneck [54] in hyperviscous simulations is visible in the statistics of the SFS energy transfer. As can be seen in Figures 8(b,c), the two hyperviscous simulations H1 and H2 consistently display a much larger deviation from intermittent scaling towards the end of the inertial range compared to the Newtonian viscous simulations V1 and V2. In other words, scaling-wise there is not such a big gain by moving from normal to hyperviscosity (compare data sets V and H), unlike for the extension of the range where the total energy flux is constant (see Figure 2). Similar observations have been made in Refs. [48,49,72].

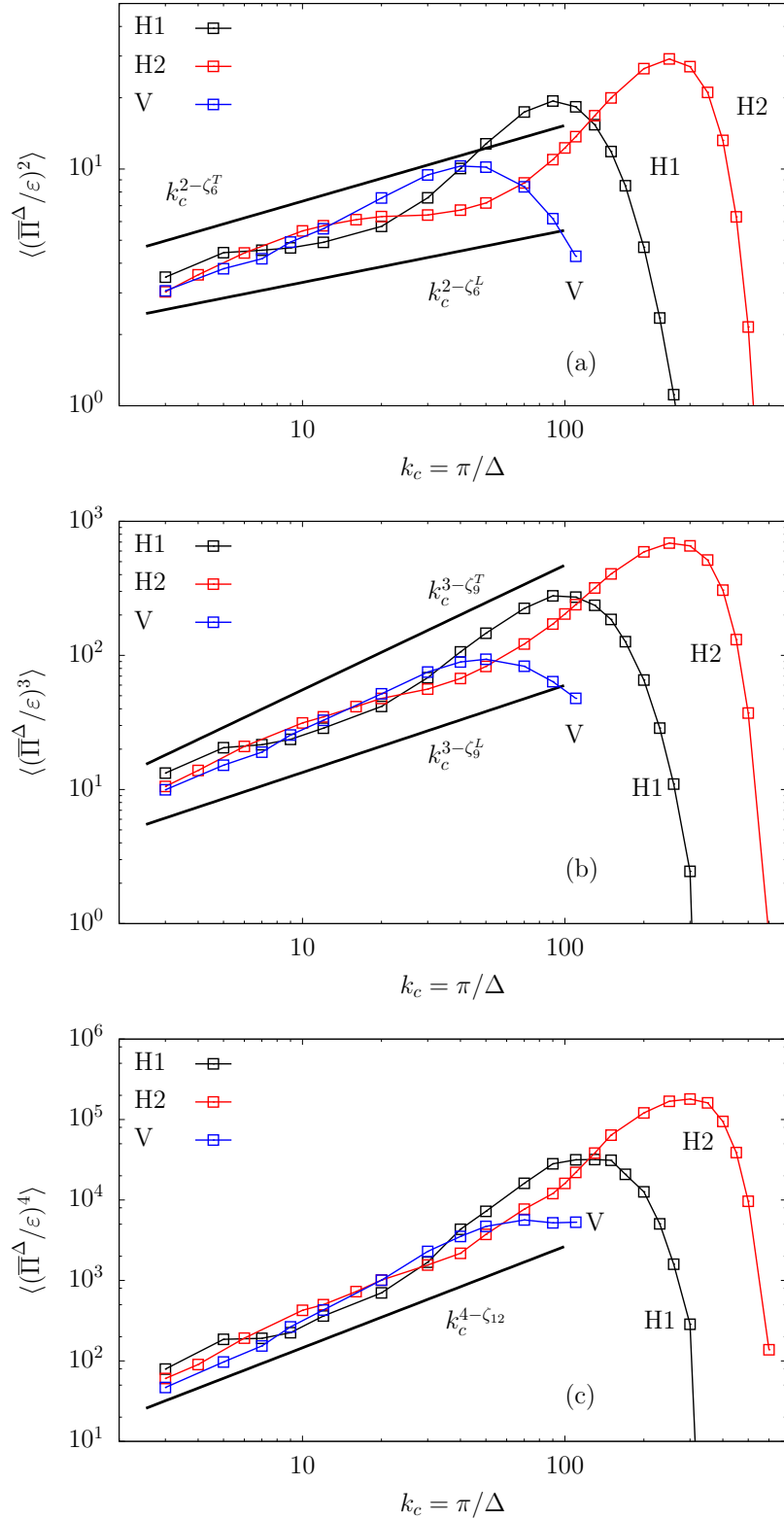


Figure 8. Scaling of the n^{th} moments of the normalised P-SFS energy transfer for data-sets V1 (blue/dark gray), V2 (green/light gray), H1 (black) and H2 (red/gray) as a function of $k_c = \pi/\Delta$, (a) $n = 2$, (b) $n = 3$, (c) $n = 4$. The solid lines indicate the scaling expected from the multifractal model and Equation (30) using the anomalous exponents for the longitudinal and transverse structure functions ζ_{3n}^L and ζ_{3n}^T , Ref. [6]. In (c) for $n = 4$ the prediction from the She-L ev eque model $\zeta_{3n} = 2.74$ [70,71] is shown.

5. Comparison of different projector filters

As pointed out in the Introduction, different filters introduce different fluctuations and the two traditional filters, Gaussian smoothing and sharp Galerkin projection, each have their own limitations. Although the Gaussian filter results in a positive definite SFS stress tensor [69] and does not induce Gibbs oscillations, it has the important limitation of not producing a clear distinction between resolved and unresolved scales. In an attempt to improve on the drawbacks of both traditional approaches of sharp Galerkin truncation and Gaussian smoothing, we introduce a new family of projector filters for which the truncation operation is carried out in a probabilistic way [73]. Specifically, the truncated modes are chosen randomly according to a probability density which decreases either linearly with increasing wavenumber:

$$\hat{G}_\Delta(\mathbf{k}) = \begin{cases} 1 & \text{for } |\mathbf{k}| < k_c \\ 1 & \text{with probability } P(k) = \frac{\lambda - k/k_c}{\lambda - 1} \text{ for } k_c < |\mathbf{k}| \leq \lambda k_c \\ 0 & \text{for } |\mathbf{k}| > \lambda k_c, \end{cases} \quad (31)$$

where $k_c = \pi/\Delta$ and $\lambda > 1$, or according to a Gaussian probability density as

$$\hat{G}_\Delta(\mathbf{k}) = 1 \quad \text{with probability } P(k) = e^{-k^2 \Delta^2}. \quad (32)$$

Two-dimensional graphical representations of all filters in Fourier space are shown in Figure 9.

The SFS energy transfer obtained through the linear probabilistic projector acting at a given threshold k_c leads to a ‘band-averaged’ Fourier-space flux

$$\langle \bar{\Pi}^\Delta \rangle = \frac{1}{(\lambda - 1)k_c} \int_{k_c}^{\lambda k_c} dk \Pi(k). \quad (33)$$

The ‘band-averaged’ Fourier flux had been introduced in Ref. [74] in order to study the locality of triadic interactions and can be obtained through a filter G_Δ whose Fourier-space profile $\hat{G}_\Delta^2(k)$ is a linearly decreasing function of k [68]. The introduction of (31) must be seen as a way to reproduce the same spectral properties of the filter proposed in [68] but with the added feature of being a projector.

The proof of Equation (33) for the linear projector follows from minor modifications of the corresponding proof of the linear filter in Ref. [68]. In the remainder of this work, the linear projector is applied with $\lambda = 2$ unless specified otherwise.

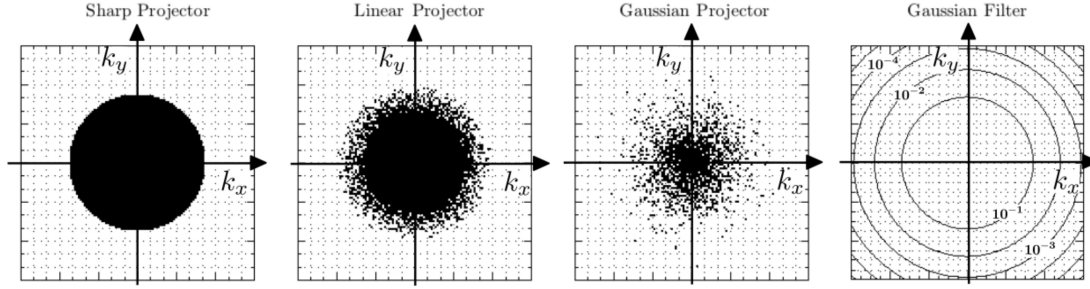


Figure 9. Two-dimensional illustration of different filters in Fourier space. From left to right: sharp Galerkin projector above k_c , Galerkin projector with a linear profile (in probability) between k_c and $2k_c$, Galerkin projector with a Gaussian profile (in probability), Gaussian filter.

We now proceed to investigate the new projectors in comparison with the sharp Galerkin projector using only the data-set H1, where for all projectors we consider the SFS-tensor corresponding to the P-SFS approach. The energy spectra obtained by different filtering procedures are presented in Figure 10(a) alongside the original unfiltered data. As can be seen, the linear projector results in a smooth roll-off of the spectrum between k_c and $2k_c$. The energy spectra obtained through Gaussian filtering and probabilistic Gaussian projection are indistinguishable, as expected. The mean SFS energy transfers obtained using the different projectors are shown in Figure 10(b) as functions of $k_c = \pi/\Delta$, in comparison with the Fourier-space energy flux $\Pi(k)$. The mean SFS energy transfer obtained from the linear projector agrees well with $\Pi(k)$ in the inertial range, as expected. The agreement is still good in the beginning of the viscous range, where $\Pi(k)$ decreases linearly and thus should coincide with $\langle \bar{\Pi}^\Delta \rangle$ obtained using the linear projector if plotted against $k = 3k_c/2$ as is the case in Figure 10(b). Deviations between the two fluxes become visible only at relatively high wavenumbers where the Fourier-flux $\Pi(k)$ decreases exponentially. The SFS energy transfer obtained from the Gaussian projector shows significant deviations from $\Pi(k)$ at low wavenumbers, while being in reasonable agreement in the inertial range. Proceeding towards the viscous range, again we observe deviations from $\Pi(k)$. Similar to the deviations between the SFS energy transfers obtained by smooth Gaussian filtering, the deviations between $\Pi(k)$ and $\langle \bar{\Pi}^\Delta \rangle$ can indeed be expected for non-sharp projector filters.

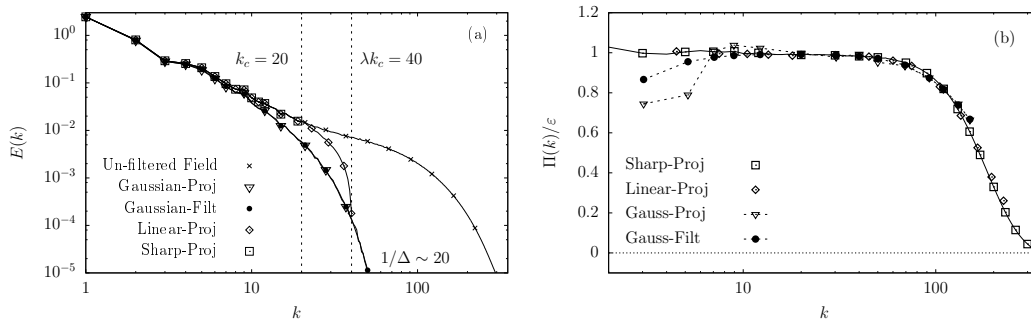


Figure 10. data-set H1. (a) Energy spectra obtained by different filtering procedures. (b) Comparison between the Fourier-space energy flux and the SFS energy transfer as a function of the cut-off wavenumber k_c for the sharp projector (squares), as a function of $3k_c/2$ for the linear projector (diamonds) and as a function of π/Δ for the Gaussian projector (triangles). The SFS energy transfer obtained through Gaussian smoothing is shown for comparison (black dots).

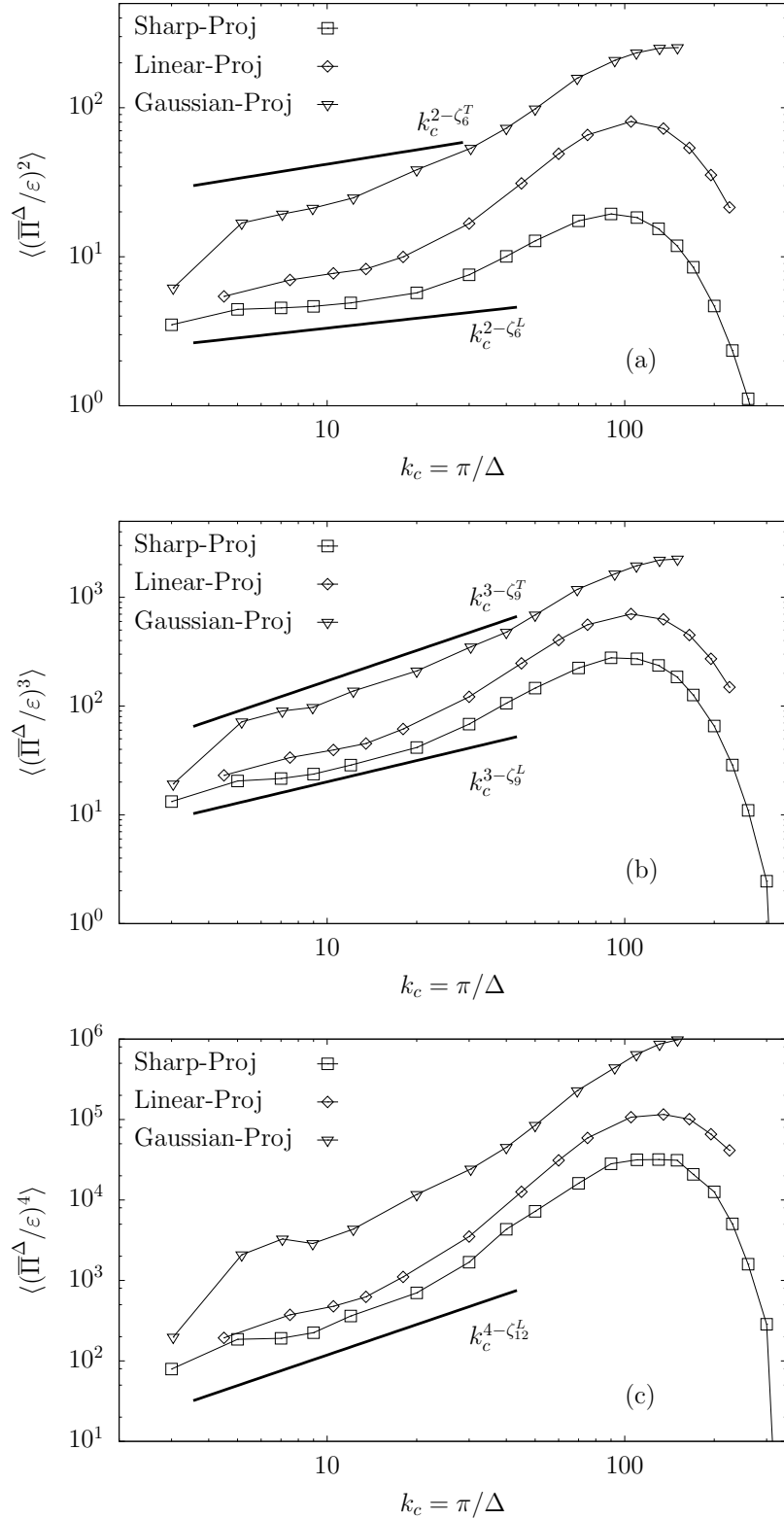


Figure 11. Scaling of the n^{th} moments of the P-SFS energy transfer for the sharp projector (squares) as a function of $k_c = \pi/\Delta$, the linear projector (diamonds) as a function of $3k_c/2$ and the Gaussian projector (triangles) as a function of π/Δ . Moments: (a) $n = 2$, (b) $n = 3$, (c) $n = 4$. The solid lines indicate the scaling expected from the multifractal model and Equation (30) using the anomalous exponents for the longitudinal and transverse structure functions ζ_{3n}^L and ζ_{3n}^T , Ref. [6]. In (c), for $n = 4$, the solid line indicates the prediction from the She-L ev eque model $\zeta_{3n} = 2.74$ [70,71] is shown.

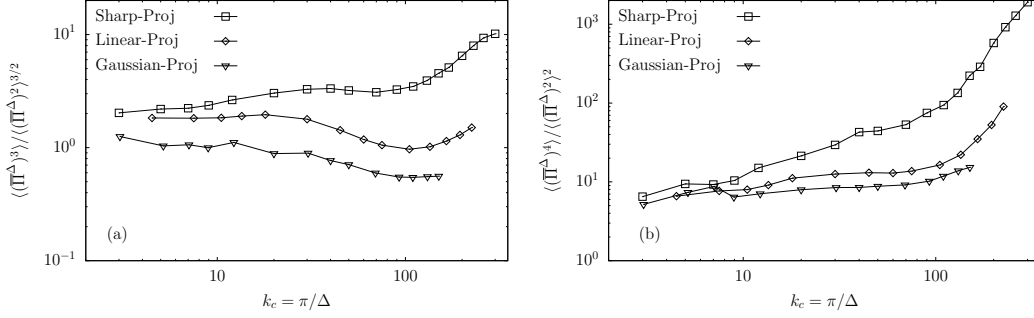


Figure 12. Skewness (a) and flatness (b) of the P-SFS energy transfer for the sharp (squares), the linear (diamonds) and the Gaussian (triangles) projectors for data-set H1. The solid lines in (a) indicate the scaling expected from the multifractal model and Equation (30) using the anomalous exponents for the longitudinal and transverse structure functions ζ_{3n}^L and ζ_{3n}^T , Ref. [6].

Concerning the multiscale statistics of the P-SFS energy transfer $\bar{\Pi}^\Delta$ for the different projectors, the non-sharp projectors scale differently compared to the sharp projector for the symmetric part $\langle (\bar{\Pi}^\Delta)^2 \rangle$ as shown in Figure 11(a), while all projectors display similar scaling for the asymmetric part $\langle (\bar{\Pi}^\Delta)^3 \rangle$ and for $\langle (\bar{\Pi}^\Delta)^4 \rangle$ as shown in Figures 11 (b-c). In particular, the scaling of $\langle (\bar{\Pi}^\Delta)^2 \rangle$ obtained using the Gaussian projector deviates significantly from the intermittent scaling displayed by $\langle (\bar{\Pi}^\Delta)^2 \rangle$ obtained by sharp Galerkin projection. The difference in the scaling of $\langle (\bar{\Pi}^\Delta)^2 \rangle$ between the different projectors propagates into the scaling of skewness and flatness as shown in Figures 12(a,b)

The deviation from intermittent scaling of skewness and flatness of the SFS energy transfers for the linear and Gaussian projectors may be connected to their higher degree of discontinuity in Fourier space. Previous studies [73,75,76] showed that a removal of the degrees of freedom results in a decrease in intermittency. Such removal of the degrees of freedom can be carried out either by a dynamic procedure where the corresponding projection operation is carried out at each iteration step, or by one-off projection carried out on the DNS data obtained by evolving the full Navier Stokes equations. The latter is referred to as static decimation. The dynamic fractal projection operation generally leads to a drastic decrease in intermittency, where the removal of a small percentage of Fourier modes already results in near-Gaussian statistics at all scales. Intermittency is also decreased by static decimation [75], however, compared to the dynamic procedure a much larger percentage of modes must be removed. The probabilistic filtering applied here could be seen as a static decimation carried out in logarithmically spaced Fourier bands, where at least towards the middle of the wavenumber band a significant percentage of Fourier modes will have been removed. A non-sharp projector has also the disadvantage of increasing the frontier in Fourier space among resolved and unresolved modes and it induces further discontinuities in Fourier space through the probabilistic projection operation. As such, Gibbs oscillations in real space are enhanced, perhaps one of the reasons for the reduction in intermittency. These properties might not necessarily be detrimental for the implementation of *a posteriori* SFS stress models on such a non-traditional Fourier support. The effects of the SFS stress tensor on the dynamical evolution of the resolved scale can be summarised in a multiscale correlation function among velocity increments $\delta_r \mathbf{v}$ and the SFS tensor $\tau(\Delta)$ with $r > \Delta$ (see [27] for a discussion concerning the evolution of second order correlation functions of the resolved field), and it remains to be

checked by explicit LES performed on different Fourier supports how to minimise the feedback in order to enhance the extension of the inertial range. Work in this direction will be reported elsewhere.

6. Conclusions

In this paper, we have studied the statistical properties of SFS energy transfer in the inertial range of scales with particular emphasis on the effect of the filtering procedure using approaches based on Gaussian smoothing, sharp Galerkin projections and new multiscale projectors. We discuss formal and practical advantages/disadvantages of projector filters and we discuss a LES formalism which is Galilean invariant and mathematically well defined. In order to assess the multiscale statistics and the related scaling estimates, we carried out an *a priori* analysis of the SFS energy transfer obtained through different filtering procedures using high-resolution DNS data-sets with normal as well as hyperviscosity on up to 2048^3 collocation points. We extend known results for the scaling properties of the SFS energy transfer using Gaussian smoothing [47,68] to the case of sharp projector filters relating the scaling exponents of the SFS energy transfer to the anomalous exponents of the velocity structure functions. We find that the SFS energy transfer is sensitive to intermittent effects. Although the intermittent scaling of SFS energy transfer appears to be sensitive to the additional oscillations induced by the probabilistic projectors, the effects of different filtering protocols on *a posteriori* LES simulations remain to be studied. It may even be conceivable that a filter which induces more oscillations in physical space results in a decorrelation effect between the resolved scales and the scales close to the filter threshold which are most affected by the choice of filtering strategy. Our results can be regarded as a systematic assessment of the impacts of using projectors or filters on the multiscale properties of turbulence at high Reynolds numbers and prompt for the need to perform suitable LES *a posteriori* studies to benchmark the validity of different subgrid models to reproduce those properties.

Acknowledgements

The research leading to these results has received funding from the European Union's Seventh Framework Programme (FP7/2007-2013) under grant agreement No. 339032 and from COST ACTION (MP 1305). H. Aluie was also supported through NSF grant OCE-1259794, DOE grants de-sc0014318 and DE-561 NA0001944, and the LANL LDRD program through project number 20150568ER. J. Brasseur was supported by AFOSR Grant FA9550-16-0388. C. Meneveau was supported by the National Science Foundation (CBET 1507469).

Appendix A. Galilean invariance

We consider a Galilean transformation

$$x_i \rightarrow x_i - u_i^0 t, \tag{A1}$$

such that

$$v_i \rightarrow v_i + u_i^0, \quad (\text{A2})$$

with a spatially uniform and time-independent u_i^0 . The aim is to establish (i) the breaking of Galilean invariance of the SFS stress tensor induced by additional filtering of the inertial term by a non-projector filter, and (ii) the pointwise global Galilean invariance on the level the kinetic energy for the P-SFS approach.

A.1. *Breaking of Galilean invariance of the SFS stress tensor for non-projector filters*

We consider the momentum balance for the resolved field \tilde{v} with a filtered inertial term

$$\partial_t \tilde{v}_i + \partial_j (\widetilde{\tilde{v}_i \tilde{v}_j} + \tilde{p} \delta_{ij} + \tilde{\tau}_{ij}^\Delta) = 0. \quad (\text{A3})$$

Under the Galilean transformation given by Equations (A1) and (A2), this equation becomes

$$\partial_t [\tilde{v}_i(\mathbf{x} - \mathbf{u}^0 t, t) + u_i^0] + \partial_j \left(\overline{(\tilde{v}_j + u_j^0)(\tilde{v}_i + u_i^0)} + \tilde{p} \delta_{ij} + \tilde{\tau}_{ij}^\Delta(\mathbf{v} + \mathbf{u}^0, \mathbf{v} + \mathbf{u}^0) \right) = 0. \quad (\text{A4})$$

The subgrid tensor $\tilde{\tau}_{ij}^\Delta$, which, unlike in the main text, in this appendix originates from the *filtered* inertial term, i.e., $\tilde{\tau}_{ij}^\Delta = \widetilde{\tilde{v}_i \tilde{v}_j} - \tilde{v}_i \tilde{v}_j$ is now not Galilean invariant since

$$\begin{aligned} \tilde{\tau}_{ij}^\Delta(\mathbf{v} + \mathbf{u}^0, \mathbf{v} + \mathbf{u}^0) &= \overline{(v_i + u_i^0)(v_j + u_j^0)} - \overline{(\tilde{v}_i + u_i^0)(\tilde{v}_j + u_j^0)} \\ &= \overline{v_i v_j} + \tilde{v}_i u_j^0 + \tilde{v}_j u_i^0 + u_i^0 u_j^0 - (\widetilde{\tilde{v}_i \tilde{v}_j} + \tilde{v}_i u_j^0 + \tilde{v}_j u_i^0 + u_i^0 u_j^0) \\ &= \overline{v_i v_j} - \widetilde{\tilde{v}_i \tilde{v}_j} + (\tilde{v}_j - \tilde{v}_j) u_i^0 + (\tilde{v}_i - \tilde{v}_i) u_j^0 \neq \tilde{\tau}_{ij}^\Delta(\mathbf{v}, \mathbf{v}). \end{aligned} \quad (\text{A5})$$

Equation (A4) is still *globally* Galilean invariant, since

$$\begin{aligned} \partial_t \tilde{v}_i - u_j^0 \partial_j \tilde{v}_i + \partial_j (\widetilde{\tilde{v}_j \tilde{v}_i} + u_j^0 \tilde{v}_i + u_i^0 \tilde{v}_j + \tilde{v}_i u_j^0 + \tilde{v}_j u_i^0 + \tilde{p} \delta_{ij} + \tilde{\tau}_{ij}^\Delta \\ + (\tilde{v}_j - \tilde{v}_j) u_i^0 + (\tilde{v}_i - \tilde{v}_i) u_j^0) = 0, \end{aligned} \quad (\text{A6})$$

where we recover Equation (A3) because $-u_j^0 \partial_j \tilde{v}_i$ cancels with $\partial_j (u_j^0 \tilde{v}_i)$, $\partial_j (u_i^0 \tilde{v}_j) = 0$ by incompressibility of \tilde{v} and the double-filtered terms cancel out. For projector filters, we can see directly from Equation (A5) that $\tilde{\tau}_{ij}^\Delta$ is Galilean invariant since the terms of the form $\overline{v} - \widetilde{\tilde{v}}$ vanish identically because $G^2 = G$.

A.2. *Global Galilean invariance of the P-SFS energy balance*

The balance equation for the total resolved energy in the P-SFS approach is

$$\frac{1}{2} \partial_t (\overline{v_i v_i}) + \partial_j (\overline{v_i (\overline{v_j v_i} + \tilde{p} \delta_{ij} + \tilde{\tau}_{ij}^\Delta)}) = -\overline{\Pi}^\Delta + (\partial_j \overline{v_i})(\overline{v_j v_i}). \quad (\text{A7})$$

Under the Galilean transformation given by Equations (A1) and (A2), Equation (A7) becomes

$$\begin{aligned} \frac{1}{2} \partial_t [\bar{v}_i(\mathbf{x} - \mathbf{u}^0 t, t) + u_i^0]^2 + \partial_j \left((\bar{v}_i + u_i^0) \left[\overline{(\bar{v}_j + u_j^0)(\bar{v}_i + u_i^0)} + \bar{p} \delta_{ij} + \bar{\tau}_{ij}^\Delta \right] \right) \\ = -\bar{\Pi}^\Delta + (\partial_j (\bar{v}_i + u_i^0)) \overline{(\bar{v}_j + u_j^0)(\bar{v}_i + u_i^0)}, \end{aligned} \quad (\text{A8})$$

where we used the fact that $\bar{\Pi}^\Delta$ and τ_{ij}^P are Galilean invariant. We now calculate the remaining terms in Equation (A8) explicitly. The terms on the LHS are

$$\begin{aligned} \frac{1}{2} \partial_t [\bar{v}_i(\mathbf{x} - \mathbf{u}^0 t, t) + u_i^0]^2 &= (\bar{v}_i + u_i^0) \partial_t \bar{v}_i(\mathbf{x} - \mathbf{u}^0 t, t) = (\bar{v}_i + u_i^0) (\partial_t \bar{v}_i - u_j^0 \partial_j \bar{v}_i) \\ &= \bar{v}_i \partial_t \bar{v}_i + u_i^0 \partial_t \bar{v}_i - \bar{v}_i u_j^0 \partial_j \bar{v}_i - u_i^0 u_j^0 \partial_j \bar{v}_i, \end{aligned} \quad (\text{A9})$$

and

$$\begin{aligned} \partial_j \left((\bar{v}_i + u_i^0) \overline{(\bar{v}_j + u_j^0)(\bar{v}_i + u_i^0)} \right) &= \partial_j (\bar{v}_i \overline{\bar{v}_j \bar{v}_i}) + 2u_i^0 u_j^0 \partial_j \bar{v}_i + u_j^0 \partial_j (\bar{v}_i \bar{v}_i) \\ &\quad + u_i^0 \bar{v}_j \partial_j \bar{v}_i + u_i^0 \partial_j \overline{(\bar{v}_i \bar{v}_j)}, \end{aligned} \quad (\text{A10})$$

using incompressibility of \mathbf{v} . The remaining term on the RHS of Equation (A7) is

$$(\partial_j (\bar{v}_i + u_i^0)) \overline{(\bar{v}_j + u_j^0)(\bar{v}_i + u_i^0)} = \overline{\bar{v}_j \bar{v}_i} + \bar{v}_i u_j^0 + \bar{v}_j u_i^0 + u_i^0 u_j^0 \partial_j \bar{v}_i. \quad (\text{A11})$$

By substitution of the relevant terms with their explicit expressions given in Equations (A9)-(A11), the kinetic energy budget Equation (A7) becomes

$$\begin{aligned} &\bar{v}_i \partial_t \bar{v}_i + u_i^0 \partial_t \bar{v}_i - \bar{v}_i u_j^0 \partial_j \bar{v}_i - u_i^0 u_j^0 \partial_j \bar{v}_i \\ &\quad + \partial_j (\bar{v}_i \overline{\bar{v}_j \bar{v}_i}) + 2u_i^0 u_j^0 \partial_j \bar{v}_i + u_j^0 \partial_j (\bar{v}_i \bar{v}_i) + u_i^0 \bar{v}_j \partial_j \bar{v}_i + u_i^0 \partial_j \overline{(\bar{v}_i \bar{v}_j)} \\ &\quad + \partial_j (\bar{v}_i \tau_{ij}^P) + u_i^0 \partial_j \tau_{ij}^P + \partial_j (\bar{v}_i \bar{p} \delta_{ij}) + u_i^0 \partial_j \bar{p} \delta_{ij} \\ &= \overline{\bar{v}_j \bar{v}_i} \partial_j \bar{v}_i + \bar{v}_i u_j^0 \partial_j \bar{v}_i + \bar{v}_j u_i^0 \partial_j \bar{v}_i + u_i^0 u_j^0 \partial_j \bar{v}_i - \bar{\Pi}^\Delta, \end{aligned} \quad (\text{A12})$$

which can be rearranged to

$$\begin{aligned} \frac{1}{2} \partial_t (\bar{v}_i)^2 + \partial_j (\bar{v}_i (\overline{\bar{v}_j \bar{v}_i} + \bar{p} \delta_{ij} + \bar{\tau}_{ij}^\Delta)) + u_i^0 (\partial_t \bar{v}_i + \partial_j (\overline{\bar{v}_i \bar{v}_j} + \bar{p} \delta_{ij} + \tau_{ij}^P)) \\ = \overline{\bar{v}_j \bar{v}_i} \partial_j \bar{v}_i - \bar{\Pi}^\Delta, \end{aligned} \quad (\text{A13})$$

where we observe that $u_i^0 (\partial_t \bar{v}_i + \partial_j (\overline{\bar{v}_i \bar{v}_j} + \bar{p} \delta_{ij} + \tau_{ij}^P)) = 0$ from the P-SFS momentum equation. Hence we recover Equation (A7)

$$\frac{1}{2} \partial_t (\bar{v}_i)^2 + \partial_j (\bar{v}_i (\overline{\bar{v}_j \bar{v}_i} + \bar{p} \delta_{ij} + \bar{\tau}_{ij}^\Delta)) = \overline{\bar{v}_j \bar{v}_i} \partial_j \bar{v}_i - \bar{\Pi}^\Delta, \quad (\text{A14})$$

and conclude that the P-SFS kinetic energy evolution equation is globally Galilean invariant.

Appendix B. Scaling estimates for projector filters

In this appendix we show that Eyink's proof of Equation (30) in Ref. [47] for the F-SFS energy flux extends to the P-SFS flux by approximating the sharp Galerkin projector with a smooth filter to arbitrary accuracy. This statement will be made more precise in the following. For convenience, we work in \mathbb{R}^n . First we establish that Equation (30) holds in approximation for the F-SFS formulation and then extend the result to the P-SFS formulation. Let $S(\mathbb{R}^n)$ be the Schwartz class of all smooth functions whose derivatives tend to zero faster than any power. The elements of $S(\mathbb{R}^n)$ themselves also decrease sufficiently fast at infinity. Schwartz functions therefore satisfy all the regularity requirements for filters which were necessary in the proof of Equation (30) carried out in Ref.[47]. The Schwartz class also has the useful property that the Fourier transform maps $S(\mathbb{R}^n)$ to itself (it is an automorphism on $S(\mathbb{R}^n)$). In order to find a smooth filter that approximates the sharp projector \hat{G}_Δ , it suffices to use a standard result from functional analysis, namely that $S(\mathbb{R}^n) \subset L^p(\mathbb{R}^n)$ as a dense subspace for $1 \leq p < \infty$. Hence if $f \in L^p(\mathbb{R}^n)$ for $1 \leq p < \infty$ then we can always find a function $f^\varepsilon \in S(\mathbb{R}^n)$ such that

$$\|f^\varepsilon - f\|_p < \varepsilon_p \quad \text{for } 1 \leq p < \infty, \quad (\text{B1})$$

for any $\varepsilon_p > 0$. For the standard projector $\hat{G}_\Delta = \theta(k_c - |\mathbf{k}|)$, where θ is the Heaviside step function, it is immediately clear that $\hat{G}_\Delta \in L^p(\mathbb{R}^n)$ for $1 \leq p \leq \infty$, and its inverse Fourier transform satisfies $G_\Delta \in L^p(\mathbb{R}^n)$ for $2 \leq p \leq \infty$. This implies that we can always find $G_\Delta^\varepsilon \in S(\mathbb{R}^n)$ such that

$$\|G_\Delta^\varepsilon - G_\Delta\|_p < \varepsilon_p \quad \text{for } 2 \leq p < \infty. \quad (\text{B2})$$

Hence we can always approximate the projector filter with a smooth filter which satisfies the scaling estimate Equation (30) for the F-SFS fomulation.

The only difference between the P-SFS and the F-SFS formulations is in the definition of the SFS stress tensor

$$\begin{aligned} \bar{\tau}^\Delta(\mathbf{v}, \mathbf{v}) &= \overline{\mathbf{v} \otimes \mathbf{v}} - \overline{\bar{\mathbf{v}} \otimes \bar{\mathbf{v}}} = \overline{\mathbf{v} \otimes \mathbf{v}} - \bar{\mathbf{v}} \otimes \bar{\mathbf{v}} - (\overline{\bar{\mathbf{v}} \otimes \bar{\mathbf{v}}} - \bar{\mathbf{v}} \otimes \bar{\mathbf{v}}) \\ &= \underbrace{\overline{\mathbf{v} \otimes \mathbf{v}} - \bar{\mathbf{v}} \otimes \bar{\mathbf{v}}}_{\text{F-SFS}} - \underbrace{(\overline{\bar{\mathbf{v}} \otimes \bar{\mathbf{v}}} - \bar{\mathbf{v}} \otimes \bar{\mathbf{v}})}_{\text{Leonard stress}} + (\bar{\mathbf{v}} \otimes \bar{\mathbf{v}} - \overline{\bar{\mathbf{v}} \otimes \bar{\mathbf{v}}}), \end{aligned} \quad (\text{B3})$$

where the Leonard stress has been decomposed into two components, the last of which does not vanish in the present case since (\cdot) here refers to the filtering by G_Δ^ε which is not a projector. According to Ref. [47] Equation (81), the F-SFS component satisfies

$$\|\overline{\mathbf{v} \otimes \mathbf{v}} - \bar{\mathbf{v}} \otimes \bar{\mathbf{v}}\|_p = O(\Delta^{2\zeta_{2p}/p}). \quad (\text{B4})$$

The term $\overline{\bar{\mathbf{v}} \otimes \bar{\mathbf{v}}} - \bar{\mathbf{v}} \otimes \bar{\mathbf{v}}$ has also been considered in Ref. [47] in connection with the infrared locality of the F-SFS stress tensor. In particular, Equation (99) of Ref. [47] implies

$$\|\overline{\bar{\mathbf{v}} \otimes \bar{\mathbf{v}}} - \bar{\mathbf{v}} \otimes \bar{\mathbf{v}}\|_p = O(\Delta^{2\zeta_{2p}/p}). \quad (\text{B5})$$

Hence two out of the three terms on the RHS of Equation (B3) have the desired scaling properties. In order to obtain the scaling for $\bar{\tau}^\Delta(\mathbf{v}, \mathbf{v})$ we must consider the L^p -norm of the remaining term $\bar{\mathbf{v}} \otimes \bar{\mathbf{v}} - \bar{\bar{\mathbf{v}}} \otimes \bar{\bar{\mathbf{v}}}$ for the filter G_Δ^ε

$$\begin{aligned} \|\bar{\mathbf{v}} \otimes \bar{\mathbf{v}} - \bar{\bar{\mathbf{v}}} \otimes \bar{\bar{\mathbf{v}}}\|_p &= \frac{1}{2} (\|(\bar{\mathbf{v}} - \bar{\bar{\mathbf{v}}}) \otimes (\bar{\mathbf{v}} + \bar{\bar{\mathbf{v}}}) + (\bar{\mathbf{v}} + \bar{\bar{\mathbf{v}}}) \otimes (\bar{\mathbf{v}} - \bar{\bar{\mathbf{v}}})\|_p) \\ &\leq \|(\bar{\mathbf{v}} - \bar{\bar{\mathbf{v}}})\|_{2p} \|(\bar{\mathbf{v}} + \bar{\bar{\mathbf{v}}})\|_{2p} \\ &\leq \|G_\Delta^\varepsilon - (G_\Delta^\varepsilon * G_\Delta^\varepsilon)\|_2 \|G_\Delta^\varepsilon + (G_\Delta^\varepsilon * G_\Delta^\varepsilon)\|_2 \|\mathbf{v}\|_r^2, \end{aligned} \quad (\text{B6})$$

where in the last step we used Young's inequality with $r = 2p/(p+1)$ combined with the fact that $G_\Delta^\varepsilon \in S(\mathbb{R}^n)$, since this implies that $(G_\Delta^\varepsilon * G_\Delta^\varepsilon) \in S(\mathbb{R}^n)$ and $G_\Delta^\varepsilon \in L^p(\mathbb{R}^n)$ for $2 \leq p \leq \infty$. The same holds for $(G_\Delta^\varepsilon * G_\Delta^\varepsilon)$. The term $\|G_\Delta^\varepsilon - (G_\Delta^\varepsilon * G_\Delta^\varepsilon)\|_2 = \|\hat{G}_\Delta^\varepsilon - (\hat{G}_\Delta^\varepsilon)^2\|_2$ can now be further estimated

$$\begin{aligned} \|\hat{G}_\Delta^\varepsilon - (\hat{G}_\Delta^\varepsilon)^2\|_2 &= \|\hat{G}_\Delta^\varepsilon - \hat{G}_\Delta - ((\hat{G}_\Delta^\varepsilon)^2 - \hat{G}_\Delta)\|_2 \leq \|\hat{G}_\Delta^\varepsilon - \hat{G}_\Delta\|_2 + \|(\hat{G}_\Delta^\varepsilon)^2 - \hat{G}_\Delta\|_2 \\ &\leq \|\hat{G}_\Delta^\varepsilon - \hat{G}_\Delta\|_2 + \|\hat{G}_\Delta^\varepsilon - \hat{G}_\Delta\|_2 \|\hat{G}_\Delta^\varepsilon + \hat{G}_\Delta\|_\infty \\ &\leq \|\hat{G}_\Delta^\varepsilon - \hat{G}_\Delta\|_2 \left(1 + \|\hat{G}_\Delta^\varepsilon\|_\infty + \|\hat{G}_\Delta\|_\infty\right). \end{aligned} \quad (\text{B7})$$

where in the third step we used the Hölder inequality and the projector property $\hat{G}_\Delta^2 = \hat{G}_\Delta$. Combining Equations (B6) and (B7) results in

$$\begin{aligned} \|\bar{\mathbf{v}} \otimes \bar{\mathbf{v}} - \bar{\bar{\mathbf{v}}} \otimes \bar{\bar{\mathbf{v}}}\|_p &\leq \|\hat{G}_\Delta^\varepsilon - \hat{G}_\Delta\|_2 \left(1 + \|\hat{G}_\Delta^\varepsilon\|_\infty + \|\hat{G}_\Delta\|_\infty\right) \|G_\Delta^\varepsilon + (G_\Delta^\varepsilon * G_\Delta^\varepsilon)\|_2 \|\mathbf{v}\|_r^2 \\ &\leq C\varepsilon, \end{aligned} \quad (\text{B8})$$

with $C \equiv \|G_\Delta^\varepsilon + (G_\Delta^\varepsilon * G_\Delta^\varepsilon)\|_2 \|\mathbf{v}\|_r^2 \left(1 + \|\hat{G}_\Delta^\varepsilon\|_\infty + \|\hat{G}_\Delta\|_\infty\right)$, where we set $\varepsilon \equiv \varepsilon_2$. Since ε can be made arbitrarily small, the P-SFS formulation is expected to satisfy the same scaling estimate as the F-SFS formulation, provided the scaling suggested by the bounds in Equations (B4) and (B5) holds. While the bounds in Equations (B4) and (B5) formally diverge as G_Δ^ε approaches G_Δ , we find numerically in Figures 6 and 8 that the scaling of these bounds remains true when using a sharp Galerkin projector. After all, Equations (B4) and (B5) are upper bounds and are not necessarily tight (sharp) bounds. The L^p -norm of the SFS stress tensor can (and does) still scale according to the estimate above.

References

- [1] U. Frisch. *Turbulence: the legacy of A. N. Kolmogorov*. Cambridge University Press, 1995.
- [2] Stephen B. Pope. *Turbulent Flows*. Cambridge University Press, 2000.
- [3] M. Lesieur. *Turbulence in fluids*. Springer, 2008.
- [4] A. Arnéodo, C. Baudet, F. Belin, R. Benzi, B. Castaing, B. Chabaud, R. Chavarria, S. Ciliberto, R. Camussi, F. Chillà, B. Dubrulle, Y. Gagne, B. Hebral, J. Herweijer, M. Marchand, J. Maurer, J. F. Muzy, A. Naert, A. Noullez, J. Peinke, F. Roux, P. Tabeling, W. van de Water, and H. Willaime. Structure functions in turbulence, in various flow configurations, at Reynolds number between 30 and 5000, using extended self-similarity. *Europhys. Lett.*, 34:411–416, 1996.

- [5] J. Qian. Scaling of structure functions in homogeneous shear-flow turbulence. *Phys. Rev. E*, 65:036301, 2002.
- [6] T. Gotoh, D. Fukayama, and T. Nakano. Velocity field statistics in homogeneous steady turbulence obtained using a high-resolution direct numerical simulation. *Phys. Fluids*, 14:1065, 2002.
- [7] R. Benzi, G. Amati, C. M. Casciola, F. Toschi, and R. Piva. Intermittency and scaling laws for wall bounded turbulence. *Phys. Fluids*, 11:1284–1286, 1999.
- [8] R. A. Antonia and R. J. Smalley. Velocity and temperature scaling in a rough wall boundary layer. *Phys. Rev. E*, 62:640, 2000.
- [9] C. M. de Silva, I. Marusic, J. D. Woodcock, and C. Meneveau. Scaling of second- and higher-order structure functions in turbulent boundary layers. *J. Fluid Mech.*, 769:654–686, 2015.
- [10] A. La Porta, A. M. Crawford G. A. Voth, J. Alexander, and E. Bodenschatz. Fluid particle accelerations in fully developed turbulence. *Nature*, 409:1017–1019, 2001.
- [11] N. Mordant, P. Metz, O. Michel, and J.-F. Pinton. Measurement of Lagrangian velocity in fully developed turbulence. *Phys. Rev. Lett.*, 87:214501, 2001.
- [12] L. Biferale, G. Boffetta, A. Celani, B. J. Devenish, A. Lanotte, and F. Toschi. Multifractal statistics of Lagrangian velocity and acceleration in turbulence. *Phys. Rev. Lett.*, 93:064502, 2004.
- [13] A. Arnèodo, R. Benzi, J. Berg, L. Biferale, E. Bodenschatz, A. Busse, E. Calzavarini, B. Castaing, M. Cencini, L. Chevillard, R. T. Fisher, R. Grauer, H. Homann, D. Lamb, A. S. Lanotte, E. Lévêque, B. Lüthi, J. Mann, N. Mordant, W.-C. Müller, S. Ott, N. T. Ouellette, J.-F. Pinton, S. B. Pope, S. G. Roux, F. Toschi, H. Xu, and P. K. Yeung. Universal Intermittent Properties of Particle Trajectories in Highly Turbulent Flows. *Phys. Rev. Lett.*, 100:254504, 2008.
- [14] F. Toschi and E. Bodenschatz. Lagrangian properties of particles in turbulence. *Annu. Rev. Fluid Mech.*, 41:375–404, 2009.
- [15] R. Benzi, L. Biferale, R. Fisher, D. Q. Lamb, and F. Toschi. Inertial range Eulerian and Lagrangian statistics from numerical simulations of isotropic turbulence. *J. Fluid Mech.*, 653:221–244, 2010.
- [16] J. Smagorinsky. General circulation experiments with the primitive equations: I. the basic experiment. *Monthly weather review*, 91:99–164, 1963.
- [17] C. Meneveau and J. Katz. Scale-invariance and turbulence models for large-eddy simulation. *Ann. Rev. Fluid Mech.*, 32:1, 2000.
- [18] P. Sagaut and C. Cambon. *Homogeneous Turbulence Dynamics*. Cambridge University Press, Cambridge, 2008.
- [19] Ugo Piomelli, Parviz Moin, and Joel H. Ferziger. Model consistency in large eddy simulation of turbulent channel flows. *Phys. Fluids*, 31:1884–1891, 1988.
- [20] Yong Zhou, James G Brasseur, and Anurag Juneja. A resolvable subfilter-scale model specific to large-eddy simulation of under-resolved turbulence. *Physics of Fluids*, 13(9):2602–2610, 2001.
- [21] James G. Brasseur and Tie Wei. Designing large-eddy simulation of the turbulent boundary layer to capture law-of-the-wall scaling. *Phys. Fluids*, 22:021303, 2010.
- [22] C. Meneveau and I. Marusic. Generalized logarithmic law for high-order moments in turbulent boundary layers. *J. Fluid Mech.*, 719:R1, 2013.
- [23] Leo H. O. Hellström, Ivan Marusic, and Alexander J. Smits. Self-similarity of the large-scale motions in turbulent pipe flow. *Journal of Fluid Mechanics*, 792:R1, 2016.
- [24] X. I. A. Yang, C. Meneveau, I. Marusic, and L. Biferale. Extended self-similarity in moment-generating-functions in wall-bounded turbulence at high reynolds number. *Phys. Rev. Fluids*, 1:044405, 2016.
- [25] R. J. A. M. Stevens, M. Wilczek, and C. Meneveau. Large-eddy simulation study of the logarithmic law for second- and higher-order moments in turbulent wall-bounded flow. *J. Fluid Mech.*, 757:888–907, 2014.
- [26] L. A. Martínez Tossas, M. J. Churchfield, and C. Meneveau. A Highly Resolved Large-

- Eddy Simulation of a Wind Turbine using an Actuator Line Model with Optimal Body Force Projection. *Journal of Physics: Conference Series*, 753:082014, 2016.
- [27] C. Meneveau. Statistics of turbulence subgrid-scale stresses: Necessary conditions and experimental tests. *Phys. Fluids*, 6:815, 1994.
- [28] F. Waleffe. The nature of triad interactions in homogeneous turbulence. *Phys. Fluids A*, 4:350–363, 1992.
- [29] C. M. Casciola, P. Gualteru, R. Benzi, and R. Piva. Scale-by-scale budget and similarity laws for shear turbulence. *J. Fluid Mech.*, 476:105–114, 2003.
- [30] L. Fang, W. J. T. Bos, L. Shao, and J.-P. Bertoglio. Time reversibility of Navier–Stokes turbulence and its implication for subgrid scale models. *J. Turbulence*, 13:N3, 2012.
- [31] L. Biferale, S. Musacchio, and F. Toschi. Inverse energy cascade in three-dimensional isotropic turbulence. *Phys. Rev. Lett.*, 108:164501, 2012.
- [32] Q. Chen, S. Chen, and G. L. Eyink. The joint cascade of energy and helicity in three-dimensional turbulence. *Phys. Fluids*, 15:361, 2003.
- [33] Q. Chen, S. Chen, G. L. Eyink, and D. D. Holm. Intermittency in the Joint Cascade of Energy and Helicity. *Phys. Rev. Lett.*, 90:214503, 2003.
- [34] L. M. Smith, J. R. Chasnov, and F. Waleffe. Crossover from Two- to Three-Dimensional Turbulence. *Phys. Rev. Lett.*, 77:2467, 1996.
- [35] P. D. Mininni, A. Alexakis, and A. G. Pouquet. Scale interactions and scaling laws in rotating flows at moderate rossby numbers and large reynolds numbers. *Phys. Fluids*, 21:015108, 2009.
- [36] L. Biferale, F. Bonaccorso, I. M. Mazzitelli, M. A. T. van Hinsberg, A. S. Lanotte, S. Musacchio, P. Perlekar, and F. Toschi. Coherent Structures and Extreme Events in Rotating Multiphase Turbulent Flows. *Phys. Rev. X*, 6:041036, 2016.
- [37] G. D. Nastrom, K. S. Gage, and W. H. Jasperson. Kinetic energy spectrum of large- and mesoscale atmospheric processes. *Nature*, 310:36–38, 1984.
- [38] M. Lautenschlager, D. P. Eppel, and W. C. Thacker. Subgrid parametrization in helical flows. *Beitr. Phys. Atmosph.*, 61:87–97, 1988.
- [39] L. M. Smith and F. Waleffe. Transfer of energy to two-dimensional large scales in forced, rotating three-dimensional turbulence. *Phys. Fluids*, 11:1608, 1999.
- [40] A. Celani, S. Musacchio, and D. Vincenzi. Turbulence in More than Two and Less than Three Dimensions. *Phys. Rev. Lett.*, 104:184506, 2010.
- [41] H. Xia, D. Byrne, G. Falkovich, and M. Shats. Upscale energy transfer in thick turbulent fluid layers. *Nature Physics*, 7:321, 2011.
- [42] U. Frisch, A. Pouquet, J. Léorat, and A. Mazure. Possibility of an inverse cascade of magnetic helicity in magnetohydrodynamic turbulence. *J. Fluid Mech.*, 68:769–778, 1975.
- [43] A. Pouquet, U. Frisch, and J. Léorat. Strong MHD helical turbulence and the nonlinear dynamo effect. *J. Fluid Mech.*, 77:321–354, 1976.
- [44] S. Cerutti and C. Meneveau. Intermittency and relative scaling of subgrid-scale energy dissipation in isotropic turbulence. *Phys. Fluids*, 10:928, 1998.
- [45] R. Benzi, S. Ciliberto, R. Tripiccone, C. Baudet, F. Massaioli, and S. Succi. Extended self-similarity in turbulent flows. *Phys. Rev. E*, 48:R29–R32, 1993.
- [46] R. Benzi, S. Ciliberto, C. Baudet, and G. R. Chavarria. On the scaling of three-dimensional homogeneous and isotropic turbulence. *Physica D: Nonlinear Phenomena*, 80(4):385–398, 1995.
- [47] G. L. Eyink. Locality of turbulent cascades. *Physica D*, 207:91–116, 2005.
- [48] H. Aluie and G. L. Eyink. Localness of energy cascade in hydrodynamic turbulence. I. Smooth coarse graining. *Phys. Fluids*, 21:115107, 2009.
- [49] H. Aluie and G. L. Eyink. Localness of energy cascade in hydrodynamic turbulence. II. Sharp spectral filter. *Phys. Fluids*, 21:115108, 2009.
- [50] V. Borue and S. A. Orszag. Self-similar decay of three-dimensional homogeneous turbulence with hyperviscosity. *Phys. Rev. E*, 51:2859(R), 1995.
- [51] Charles G. Speziale. Galilean invariance of subgrid-scale stress models in the large-eddy simulation of turbulence. *Journal of Fluid Mechanics*, 156:55–62, 1985.

- [52] G. S. Patterson and S. A. Orszag. Spectral Calculations of Isotropic Turbulence: Efficient Removal of Aliasing Interactions. *Phys. Fluids*, 14:2538–2541, 1971.
- [53] B. L. Sawford. Reynolds number effects in Lagrangian stochastic models of turbulent dispersion. *Phys. Fluids A*, 3:1577–1886, 1991.
- [54] G. Falkovich. Bottleneck phenomenon in developed turbulence. *Phys. Fluids*, 6(4):1411, 1994.
- [55] R. H. Kraichnan. Eddy-viscosity in two and three dimensions. *J. Atmos. Sci.*, 33:1521, 1976.
- [56] J.-P. Chollet and M. Lesieur. Parametrization of Small Scales of Three-Dimensional Isotropic Turbulence Utilizing Spectral Closures. *J. Atmos. Sci.*, 38:2747, 1982.
- [57] Daniele Carati, Grégoire S Winckelmans, and Hervé Jeanmart. On the modelling of the subgrid-scale and filtered-scale stress tensors in large-eddy simulation. *Journal of Fluid Mechanics*, 441:119–138, 2001.
- [58] Grégoire S Winckelmans, Alan A Wray, Oleg V Vasilyev, and Hervé Jeanmart. Explicit-filtering large-eddy simulation using the tensor-diffusivity model supplemented by a dynamic smagorinsky term. *Physics of Fluids*, 13(5):1385–1403, 2001.
- [59] C. R. Doering and J. D. Gibbon. *Applied Analysis of the Navier-Stokes Equations*. Cambridge University Press, 1995.
- [60] A. Leonard. Energy Cascade in Large-Eddy Simulations of Turbulent Fluid Flows. *Adv. Geophys.*, 18:237–248, 1975.
- [61] Olivier Thiry and Grégoire Winckelmans. A mixed multiscale model better accounting for the cross term of the subgrid-scale stress and for backscatter. *Physics of Fluids*, 28(2):025111, 2016.
- [62] S. S. Ray, U. Frisch, S. Nazarenko, and T. Matsumoto. Resonance phenomenon for the Galerkin-truncated Burgers and Euler equations. *Phys. Rev. E*, 84:016301, 2011.
- [63] M. K. Rivera, H. Aluie, and R. E. Ecke. The direct enstrophy cascade of two-dimensional soap film flows. *Phys. Fluids*, 26(5):055105, 2014.
- [64] K. P. Iyer, K. R. Sreenivasan, and P. K. Yeung. Reynolds number scaling of velocity increments in isotropic turbulence. *Phys. Rev. E*, 95:021101(R), 2017.
- [65] L. Biferale and I. Procaccia. Anisotropy in turbulent flows and in turbulent transport. *Phys. Rep.*, 414:43–164, 2005.
- [66] J. Schumacher, J. D. Scheel, D. Krasnov, D. A. Donzis, V. Yakhot, and K. R. Sreenivasan. Small-scale universality in fluid turbulence. *Proc. Nat. Acad. Sci. USA*, 111:10961, 2014.
- [67] P. Constantin, E. Weinan, and E. S. Titi. Onsager’s conjecture on the energy conservation for solutions of Euler’s equation. *Commun. Math. Phys.*, 165:207, 1994.
- [68] G. L. Eyink. The Multifractal Model of Turbulence and A Priori Estimates in Large-Eddy Simulation, I. Subgrid Flux and Locality of Energy Transfer. *arxiv:9602018v1*, 1996.
- [69] B. Vreman, B. Geurts, and H. Kuerten. Realizability conditions for the turbulent stress tensor in large-eddy simulation. *J. Fluid Mech.*, 278:351, 1994.
- [70] Z. S. She and E. Lévêque. Universal scaling laws in fully developed turbulence. *Phys. Rev. Lett.*, 72(3):336–339, 1994.
- [71] G. Boffetta, A. Mazzino, and A. Vulpiani. Twenty-five years of multifractals in fully developed turbulence: a tribute to Giovanni Paladin. *J. Phys. A: Math. Theor.*, 41:363001, 2008.
- [72] Uriel Frisch, Susan Kurien, Rahul Pandit, Walter Pauls, Samriddhi Sankar Ray, Achim Wirth, and Jian-Zhou Zhu. Hyperviscosity, Galerkin Truncation, and Bottlenecks in Turbulence. *Phys. Rev. Lett.*, 101:144501, 2008.
- [73] Uriel Frisch, Anna Pomyalov, Itamar Procaccia, and Samriddhi Sankar Ray. Turbulence in Noninteger Dimensions by Fractal Fourier Decimation. *Phys. Rev. Lett.*, 108:074501, 2012.
- [74] G. L. Eyink. Energy dissipation without viscosity in ideal hydrodynamics I. Fourier analysis and local energy transfer. *Physica D*, 78:222, 1994.
- [75] Alessandra S. Lanotte, Roberto Benzi, Shiva K. Malapaka, Federico Toschi, and Luca Biferale. Turbulence on a Fractal Fourier Set. *Phys. Rev. Lett.*, 115:264502, 2015.

- [76] Michele Buzzicotti, Akshay Bhatnagar, Luca Biferale, Alessandra S. Lanotte, and Samridhi Sankar Ray. Lagrangian statistics for Navier–Stokes turbulence under Fourier-mode reduction: fractal and homogeneous decimations. *New J. Physics*, 18:113047, 2016.